Research Square

Preprints are preliminary reports that have not undergone peer review.
They should not be considered conclusive, used to inform clinical practice,
or referenced by the media as validated information.

Ultra-Micro Electrodes Enable Low-Current Amplitude Discrimination in Intracortical Microstimulation

Elizabeth Su
Purdue University
Vinayak Retheesh
Duke University
Karthik Kumaravelu
Duke University
Shiva Sharma
Purdue University
Warren M. Grill
Duke University
Kevin Otto
kotto@purdue.edu

Purdue University

Article

Keywords: discrimination threshold, ultramicroelectrode, intracortical microstimulation, just noticeable difference, computational model

Posted Date: August 20th, 2026

DOI: https://doi.org/10.21203/rs.3.rs-10517334/v1

License: This work is licensed under a Creative Commons Attribution 4.0 International License.
Read Full License

Additional Declarations: No competing interests reported.

Version of Record: A version of this preprint was published at Scientific Reports on November 6th, 2026. See the published version at https://doi.org/10.1038/s41598-026-78134-9.

Ultra-Micro Electrodes Enable Low-Current Amplitude Discrimination in Intracortical Microstimulation

Elizabeth Su[1], Vinayak Retheesh[2], Karthik Kumaravelu[2], Shiva Sharma[1], Warren M. Grill[2,3,4,5], Kevin Otto[1*]

[1]Weldon School of Biomedical Engineering, Purdue University, West Lafayette, IN
[2]Department of Biomedical Engineering, Duke University, Durham, NC
[3]Department of Electrical and Computer Engineering, Duke University, Durham, NC
[4]Department of Neurobiology, Duke University, Durham, NC
[5]Department of Neurosurgery, Duke University, Durham, NC

Correspondence:
Kevin Otto, Ph.D.
Purdue University
Weldon School of Biomedical Engineering
Martin C. Jischke Hall of Biomedical Engineering
206 S. Martin Jischke Drive
West Lafayette, IN 47907-2032
kotto@purdue.edu
765 494-8273 Phone

(1) ABSTRACT:
Restoring somatosensory feedback is essential for achieving natural, embodied control of prosthetic limbs. Intracortical microstimulation (ICMS) of the somatosensory cortex can provide artificial touch by activating cortical neurons directly. Here, we systematically investigate how electrode contact size influences amplitude discrimination performance during ICMS. Six rats were chronically implanted with custom multielectrode shanks in the somatosensory cortex. Over twelve weeks, behavioral just-noticeable differences (JNDs) were quantified across eight electrode diameters (5–50 μm) using an adaptive discrimination paradigm. Discrimination thresholds were significantly lower for 5 μm and 10 μm sites than for larger contacts because these electrodes operated at lower reference stimulation amplitudes within their established charge injection safety limits. Weber fractions remained stable across electrode sizes, demonstrating proportional scaling of perceptual sensitivity with stimulus intensity. We used a biophysically realistic modeling framework to identify the underlying neural correlates of ICMS-induced amplitude discrimination. Both the magnitude of neural responses (changes in the number of activated neurons and the total population spike count) and the population mean spike count contributed to perceptual discrimination. These findings indicate that ultra-microelectrodes enable ICMS at substantially lower reference amplitudes, producing lower absolute discrimination thresholds while preserving Weber-like proportional scaling. Ultra-microelectrodes therefore preserve established psychophysical scaling while supporting low-threshold stimulation within their safe charge injection limits, enabling high-density sensory neuroprostheses.

KEYWORDS:
discrimination threshold, ultramicroelectrode, intracortical microstimulation, just noticeable difference, computational model

(2) INTRODUCTION:

Restoring somatosensation remains a substantial challenge in the development of brain–computer interfaces (BCIs) (Bensmaia & Miller 2014; Flesher et al. 2016). While modern BCIs have achieved increasingly sophisticated motor control, the absence of sensory feedback limits dexterity, embodiment, and long-term usability (Johansson & Flanagan 2009; Raspopovic et al. 2014; George et al. 2019). Intracortical microstimulation (ICMS) of the primary somatosensory cortex (S1) offers a means of evoking artificial tactile percepts by activating local neural populations and has emerged as a promising strategy for restoring sensory function (O'Doherty et al. 2011; Tabot et al. 2013; Flesher et al. 2016; Armenta Salas et al. 2018).

A key requirement for effective sensory restoration is the ability to convey graded perceptual intensity. Psychophysical performance during ICMS is often quantified using discrimination thresholds or just-noticeable differences (JNDs), which define the minimum change in stimulation intensity required to produce a perceptible difference (Romo et al. 1998; Tabot et al. 2013; Kim et al. 2015). Prior work demonstrated that ICMS-evoked perception follows principles consistent with classical sensory psychophysics, including Weber's law, suggesting that perceptual intensity scales proportionally with stimulus intensity (Romo et al. 1998; Kim et al. 2015; Bjanes & Moritz 2019; Callier et al. 2019). However, the neural and device-level factors that contribute to the absolute resolution of ICMS-based perception remain incompletely understood.

One parameter that has received comparatively limited attention is electrode contact size. Electrode geometry influences the spatial distribution of the electric field and, consequently, the population of neurons activated during stimulation (McIntyre & Grill 2001; Butovas & Schwarz 2003). Neural activation during intracortical microstimulation depends strongly on the local electric field magnitude and its spatial decay with distance from the electrode (McIntyre & Grill 2001; Wu et al. 2023). Smaller contacts are expected to generate more localized and higher-amplitude electric fields near the electrode (Newman 1966; Wiley and Webster 1982; McIntyre and Grill 2001), enabling more spatially confined axonal recruitment and potentially finer control over activation (Histed et al. 2009; Kumaravelu et al. 2022). In contrast, larger contacts distribute current over a broader area, leading to diffuse electric fields, which may drive activation patterns with reduced spatial specificity. Recent work with microscale electrodes further supports this relationship, showing that reduced electrode dimensions can produce spatially focal neural activation at substantially lower stimulation currents (Lycke et al. 2023). However, despite these well-established differences in electric field distribution and neural activation, the functional consequences of electrode contact size for perceptual discrimination during ICMS remain poorly understood, particularly in vivo. Further, the non-damaging charge injection limits of small-diameter (<10 um) disk contacts (termed ultra-micro contacts) are lower than those of larger-diameter contacts (Cogan et al. 2016), and the feasibility of using low-current stimulation through these ultra-micro contacts to evoke reliable behavioral responses remains largely unexplored.

We measured the effect of electrode contact size on amplitude discrimination performance using chronic ICMS in rat S1. Animals were implanted with multielectrode arrays containing a wide range of contact diameters (5–50 μm), allowing within-subject comparisons across electrode sizes. Behavioral discrimination thresholds were measured using an adaptive conditioned-avoidance paradigm, while stimulation parameters were tightly controlled (Koivuniemi et al. 2011; Urdaneta et al. 2021). To interpret these findings mechanistically, we complemented the experimental measurements with multiscale computational modeling to quantify activation of biophysically realistic cortical neurons.

We hypothesized that low-current stimulation through smaller electrode contacts, operated within their safe charge-injection limits, could reliably evoke behaviorally distinguishable percepts by recruiting a population of neurons through the steep potential and its gradients generated near the electrode. By integrating behavioral and modeling approaches, this work clarifies how electrode contact size and stimulus intensity jointly shape ICMS-evoked perception, with implications for the design of high-resolution sensory neuroprostheses.

(3) METHODS:

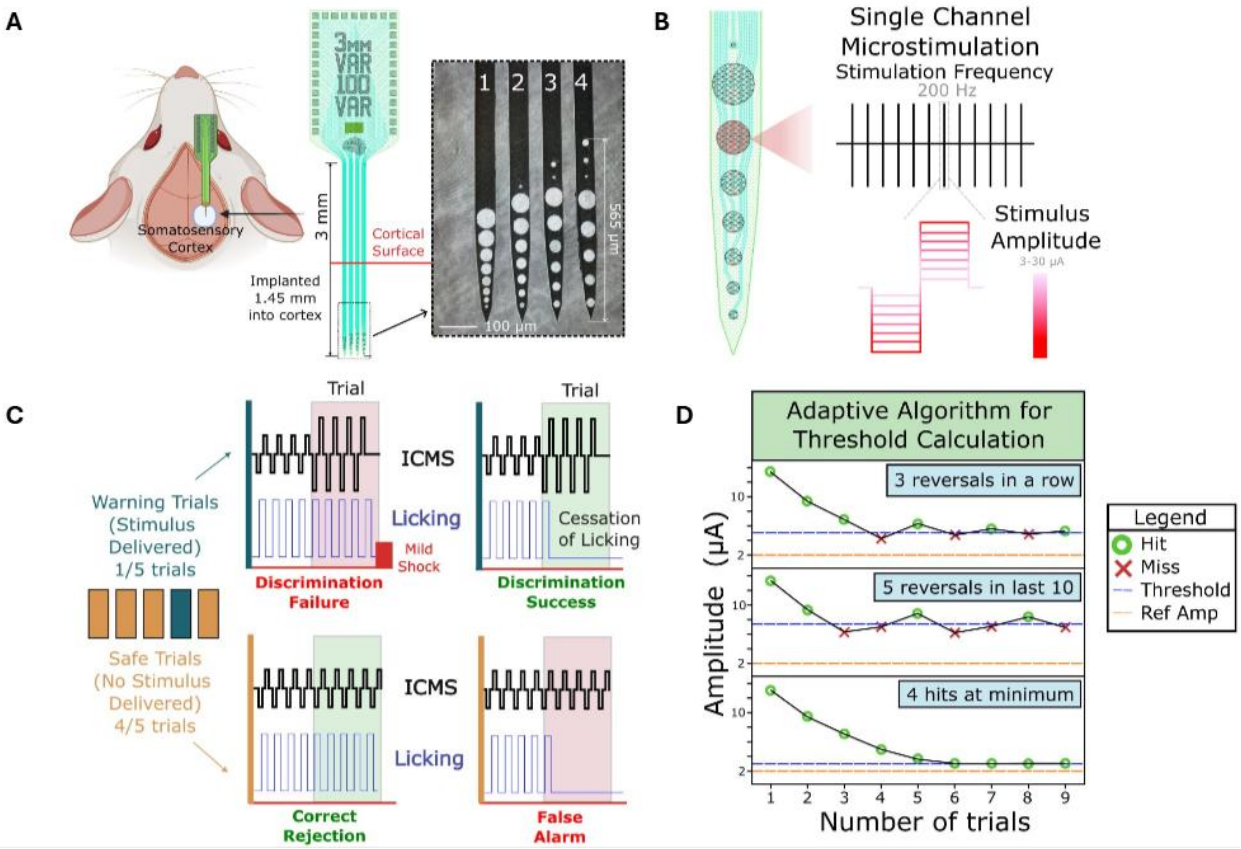


Figure 1: Overview of the G1 array design, stimulation protocol, and behavioral thresholding methods. (A) Implantation of a custom 'G1' microelectrode array (MEA) in rat somatosensory cortex, with a scanning electron microscopy (SEM) image of the G1 MEA on the right. The G1 MEA comprised four shanks, with each shank containing eight disk contacts with diameters ranging from 5 to 50 µm. (B) Single-channel ICMS parameters used throughout the experiment. Stimulation frequency, phase duration, and phase delay were held constant, while stimulus amplitude was modulated on a per-trial basis based on behavioral performance. (C) A conditioned-avoidance behavioral paradigm was used to assess the animals' ability to discriminate ICMS amplitude. Animals were required to respond appropriately to stimulation-present versus stimulation-absent trials. (D) Adaptive algorithms were used to compute discrimination thresholds. Staircase examples show how ICMS amplitude was adjusted in response to hits (green circles) and misses (red crosses). Thresholds were calculated using criteria such as three consecutive reversals, five reversals within the last ten steps, or four hits at the minimum tested amplitude.

(3.1) Device:

Custom designed planar multi-shank electrode arrays were designed by the research team and manufactured in collaboration with NeuroNexus Technologies (Ann Arbor, MI, United States) and the laboratory of Stuart Cogan at the University of Texas, Dallas (Fig 1A). Devices consisted of a silicon substrate, gold electrode traces and pads, and coated with sputtered

iridium oxide for the electrode sites (SIROF). These final devices were 3 mm in length, 15 μm in thickness, and have 8 sites per shank on 4 shanks resulting in 32 total electrodes. These sites range in diameter from 5, 10, 15, 20, 25, 30, 40, and 50 μm and have a thickness of ~1 μm.

(3.2) Surgical Procedure:

All animal experiments were conducted in accordance with the relevant guidelines set by the Institutional Animal Care and Use Committee (IACUC) of Purdue University (West Lafayette, IN, United States) under protocol 0824002520. The devices were sterilized with ethylene oxide prior to implantation. Surgeries were performed by the same surgeon throughout the study. Three male (500-600 g) and three female (250-350 g) Sprague-Dawley rats (Charles River, Chicago, IL, United States) were used for the study. Buprenorphine Ethiqa XR (0.65 mg/kg) was administered subcutaneously an hour before surgery and Meloxicam (5 mg/kg, SQ, Loxicom, Norbrook Laboratories, Newry, Northern Ireland) was administered immediately preceding the procedure. Anesthesia was induced with 3% isoflurane (Zoetis, Parsippany, NJ, United States) in oxygen at 1.5–3 L/min and maintained at 1.5–3% during surgery. The animal was held in a stereotaxic frame using ear bars. Four burr holes were drilled to secure titanium bone screws (United Titanium, Wooster, OH, United States). A cranial window (< 1 cm^2) was created over the primary somatosensory cortex (4 mm anterior to bregma, 4 mm lateral to midline) using a microdrill. The dura was reflected, and sterile saline placed on the cortex to keep it moist. A NeuroGlider (Actuated Medical, Bellefonte, PA, United States) was used to insert the microelectrode device 1,450 μm from the cortical surface to place the deepest electrode at 1,400 μm from the cortical surface. The craniotomy site was then sealed with silicon elastomer (Kwik-Sil, WPI, Sarasota, FL, United States) and layers of UV-cured dental composite (DentalSource, CA, United States) to secure the electrode array and anchor headstage connections.

(3.3) Neural Stimulation:

All microstimulation was delivered using an IZ-32 stimulator with an LZ48-200 battery (Tucker-Davis Technologies, Alachua, FL, United States) and was performed using the Synapse stimulation software from Tucker-Davis Technologies. For all experiments reported herein, stimuli were cathode-leading, charge-balanced, symmetric biphasic waveforms delivered to a single electrode site in the implanted device (Fig. 1B). Stimuli were delivered to electrode sites at 200 Hz using 650 ms pulse trains with 0.2 ms pulse duration per phase and 0.04 ms interphase interval. The total charge injected per electrode site was kept below the electrode coating damage threshold of charge density of 0.8 nC/phase for the 5 μm diameter sites and 2.4 nC/phase for the 10 μm diameter sites (Cogan et al. 2016).

(3.4) Behavioral Experiments:

Experimental sessions started after 5 days of post-surgical recovery. A modified conditioned avoidance behavioral paradigm was used to determine discrimination thresholds in rats (Fig. 1C). Water-deprived rats were placed in an isolation chamber with an instrumented metal waterspout capable of detecting contact and delivering a mild cutaneous shock. This procedure was adapted from previous studies done in our lab (Koivuniemi et al. 2011; Urdaneta et al. 2021). When the animal contacted the spout for more than 25% of a 200 ms sliding window, a trial was started. Trials were organized into five-trial blocks; four safe trials and one randomly designated warning trial. Safe trials were controlled with a familiar comparison stimulus in order to calculate false alarm rates, while warning trials stimulated the same electrode contact with a higher discrimination stimulus. Trials with a false alarm rate over 25% were discarded from analysis. Discrimination thresholds were determined with an adaptive algorithm that decreased stimulus amplitude if the animal successfully withdrew from the spout for over 20% of the stimulus presentation phase during a warning trial (“hit”) and increased if stimulus detection was unsuccessful (“miss”) (Fig. 1D). The magnitude of the change in amplitude decreased with each

trial. This pattern was repeated until three criteria were met: three reversals in a row (hit followed by miss, or vice versa), six reversals in the last ten trials or four hits at the minimum possible threshold, at which point the discrimination threshold was calculated using the average of the stimulation amplitude for the last five trials (Fig. 1D).

(3.5) Animal Euthanasia:

At the conclusion of the experimental period, animals were euthanized in accordance with protocols approved by the Purdue University Institutional Animal Care and Use Committee (IACUC) and consistent with the American Veterinary Medical Association (AVMA) Guidelines for the Euthanasia of Animals. Euthanasia was performed by carbon dioxide (CO_2) inhalation in a designated chamber, followed by decapitation using a rodent guillotine as a secondary physical method to ensure death.

(3.6) Statistical Analysis:

All statistical analyses were performed in Python using standard scientific computing libraries. Discrimination thresholds and percent-difference measures were analyzed using ordinary least squares (OLS) linear models, with electrode size, reference amplitude, animal identity, shank identity, reference group, and testing date included as predictors where appropriate. Effects of individual predictors were assessed using Type-II analyses of variance (ANOVA), which are robust to unbalanced designs and evaluate each factor after accounting for all others. Effect sizes were quantified using η^2 and partial η^2. When appropriate, simple linear regression was used to assess bivariate relationships, and post-hoc pairwise comparisons between electrode sizes were conducted with multiple-comparison correction. Statistical significance was assessed using two-tailed tests with α level of 0.05.

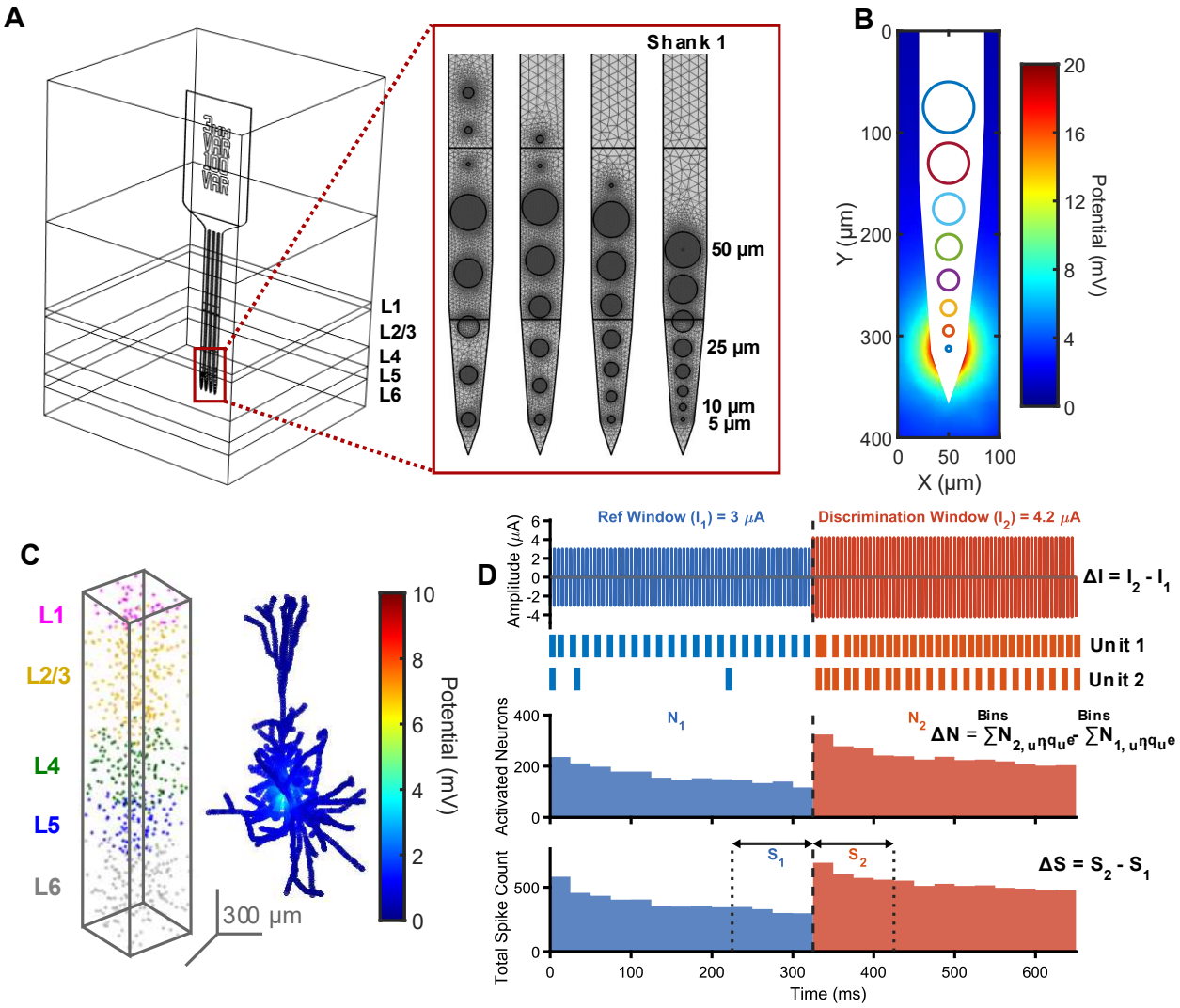


Figure 2: Computational modeling pipeline to calculate neural responses and discrimination thresholds. (A) Finite element model (FEM) of the G1 microelectrode array (MEA) and surrounding volume conductor. The volume conductor consisted of five layers (L1, L2/3, L4, L5, and L6) representing the layers within the cortical column. (B) Electric potential in the XY plane generated by stimulating the 5 µm contact with a unit (1 µA) current. The potentials on the shank are not shown to enable a voltage scale that enables visualization of the potentials in the surrounding medium. (C) Cortical column model comprising 6410 biophysically based cortical neurons with realistic (soma, dendrite, and axon) morphologies and membrane properties. The inset shows an example of a layer-5-thick tufted pyramidal neuron with electric potentials computed outside each compartment via 3D interpolation from those calculated by the FEM. (D) Intracortical microstimulation protocol to quantify discrimination threshold comprised applying two consecutive stimulus trains (reference stimulus: I_1 and discrimination stimulus: I_2) at varying intensities. The rasterogram shows firing patterns of two representative neurons. The total neural (soma) activation and total spike count across neurons were computed during the reference and discrimination windows. The differences in total neuronal activation (ΔN) and spike count (ΔS) between the discrimination and reference windows were then used to determine the model-based discrimination threshold (ΔI).

(3.7) Finite Element Model of the Electrode and Surrounding Volume Conductor:

We implemented a finite element model (FEM) of the G1 microelectrode array (MEA) and surrounding brain tissue in COMSOL Multiphysics v6.3 (COMSOL Inc., Burlington, MA). The manufacturer-provided CAD file of the G1 design was imported into COMSOL and used for subsequent simulations (Fig. 2A). The shank was modeled as a silicon (Si) insulator (conductivity: 10-12 S/m and relative permittivity: 11.7). Iridium (Ir) material (conductivity: 9.43 x 106 S/m and relative permittivity: 1) was assigned to the disk contacts. The electrode was placed in a

conducting box (2000 μm x 2000 μm x 6100 μm, Fig. 2A). The height of the box representing the cortical column (2000 μm) was divided into five layers mimicking the different layers found within a cortical column (Fig. 2A). The column thickness, relative thickness of each layer, and conductivity profile of each cortical layer were based on rat S1 (Goto et al 2010). The anisotropic conductivity assigned for each layer is shown in Table S1. The mesh was generated by assigning a growth rate such that mesh fineness decreased with distance from the active contact (Fig. 2A). The FEM consisted of 5,781,718 tetrahedral mesh elements with a minimum element quality of 0.01458 and an average element quality of 0.623.

Electric potentials were solved for each contact on shank-1 individually, with each acting as a current source, and the external (bulk tissue) boundaries were grounded (Fig. 2B). The outer boundary of the disk contact was assigned an insulator boundary condition to prevent current leakages into the shank. A point current source of 1 μA was placed at the contact center, and the discretized FEM was solved with a multifrontal massively parallel sparse direct solver (MUMPS), assuming quasi-static conditions (i.e., a stationary study) (Bossetti et al 2008) . Since the brain conductivity is linear, the potentials obtained at one current amplitude can be scaled to obtain the potentials at any other stimulation amplitude (Wang et al 2024). For simulations with different active contact diameters within shank 1, the shank position relative to the column was adjusted vertically to align the centers of each contact at the same depth in layer 5.

To assess the effect of ultra-micro (5 μm) versus micro (50 μm) contact diameters on the spatial distribution of extracellular potential, potential distributions in the XY and XZ planes were quantified (Fig. S1). Micro-scale contacts generated a broader, lower-amplitude potential distribution, whereas ultra-micro contacts produced a more localized, higher-amplitude potential distribution (Fig. S1). Further, we computed the variation in potential as a function of distance from the stimulating contact center in both lateral and normal directions (Fig. S2). The potential near the contact scaled inversely with contact diameter (Fig. S2A, B). In contrast, at distances >50 μm, the potential was largely independent of contact size, consistent with a point source approximation (Fig. S2B, D). This scaling agrees well with previous modeling and theoretical results (McIntyre & Grill 2001, Newman 1966, Wiley and Webster 1982).

(3.8) Computational Model of the Cortical Column:

The electric potentials from the FEM were coupled to a model of a cortical column (Kumaravelu et al 2022) comprising a population of neurons with realistic morphologies (Fig. 2C). Briefly, the model included 6410 biophysically based Hodgkin-Huxley-type multicompartment cortical neurons from the Blue Brain cell library, arranged in a columnar structure with five layers, 400 μm wide and 2000 μm deep. The model neurons included five different cell types: Layer (L) 1 neurogliaform cell, L 2/3 pyramidal cell, L4 large basket cell, L5 thick tufted pyramidal cell, and L6 tufted pyramidal cell. Activated neurons intersecting the electrode shank were excluded from analysis using a convex hull representation of the shank geometry. The cortical thickness and the relative thickness of each layer were based on in vitro data and matched the thickness set in the FEM. Electric potentials were evaluated at the segment centers of each compartment of the 6410 modeled neurons using COMSOL's point evaluation feature, which employs piecewise quadratic Lagrange interpolation in 3D to map the FEM-computed potentials onto the neuron geometry (Fig. 2C). The interpolated V_e from the FEM was coupled to each neuronal compartment using the $e_extracellular$ mechanism.

Simulations were implemented in NEURON v7.6 with equations solved using the backward Euler method with a time step of 25 μs. The simulation was parallelized by distributing the total number of neurons per cell type across 400 processors in a round-robin fashion.

(3.9) Modeling ICMS and Neural Data Analysis:

The ICMS protocol used to quantify discrimination thresholds in the model was similar to that used in the experiments. Briefly, stimulation comprised a 325-ms-long reference window followed by a discrimination window of the same length (Fig. 2D). To reduce computational demand, the reference and discrimination windows were shorter in the model (325 ms) than the experimental interval (650 ms). Stimulation during the 325-ms-long reference and discrimination windows was a train of biphasic pulses (cathodic first) with a fixed width of 200 μs/phase, an interphase interval of 53 μs, and a frequency of 200 Hz, identical to the experimental settings. For each contact diameter, the reference amplitude used to determine the discrimination threshold in the model was identical to that used in the experimental study (Table in Fig. 4A). We evaluated the effect of contact diameter on discrimination thresholds using a representative subset of diameters (5, 10, 25, and 50 μm). In the experimental study, each contact with a different diameter on a given shank spanned across different depths of the column. To isolate the effect of contact diameter from the column stimulation depth-dependent effect, we ensured that the centers of contact with different diameters were located at the same depth (L5) in the model (referred to as the reference depth in the subsequent sections). To assess the effect of stimulation depth on the discrimination threshold, we quantified the threshold with the contact centers shifted ±150 μm vertically from the reference depth.

One objective was to identify neural correlates of ICMS-induced discrimination thresholds in rat S1, and to this end, we quantified discrimination thresholds in the model using multiple metrics of neural activation, broadly classified into three categories:
(1) Response magnitude-based metrics, including (a) the fractional change in neural activation between reference and discrimination stimuli ($\Delta N/N_1$, Fig. 2D) the fractional change in total spike count across all activated model neurons between reference and discrimination stimuli ($\Delta S/S_1$, Fig. 2D) and (c) the product of these two metrics ($\Delta N/N_1$)*($\Delta S/S_1$). (2) Population mean-based metrics, including (a) the fractional change in mean spike count per activated neuron between reference and discrimination stimuli ($\Delta S_{mean}/S_{1,mean}$) and (b) the product of this metric and the activation metric ($\Delta S_{mean}/S_{1,mean}$)*($\Delta N/N_1$). The mean spike count per activated neuron was used in place of total spike count to isolate changes in firing rate per neuron between the reference and discrimination stimuli, independent of the number of activated neurons, thereby avoiding the redundancy introduced when combining the total spike count with a separate activation term. (3) Variance-scaled population metric, including (a) the composite of fractional change in activation and noise-normalized mean spike count change ($\Delta N/N_1$)*($\Delta S_{mean}/\sqrt{S_{1,mean}}$). The square-root scaling of the mean spike count was motivated by the Poisson-like spike statistics typically observed in cortical neurons during repeated stimulus trials, during which response variance scales with the mean (Shadlen & Newsome 1998). Although our model is deterministic, simulated spike counts can be interpreted as the mean response of an underlying stochastic neural population, in which case perceptual discrimination may be better characterized by the signal-to-noise ratio of the change in spike count between reference and discrimination stimuli, rather than by its fractional magnitude alone.

For all spike count analyses, only spikes occurring during the last 100 ms of the reference window and the first 100 ms of the discrimination window were included. This time window was chosen because it would capture the neural response transition most relevant to perceptual discrimination between two stimuli.

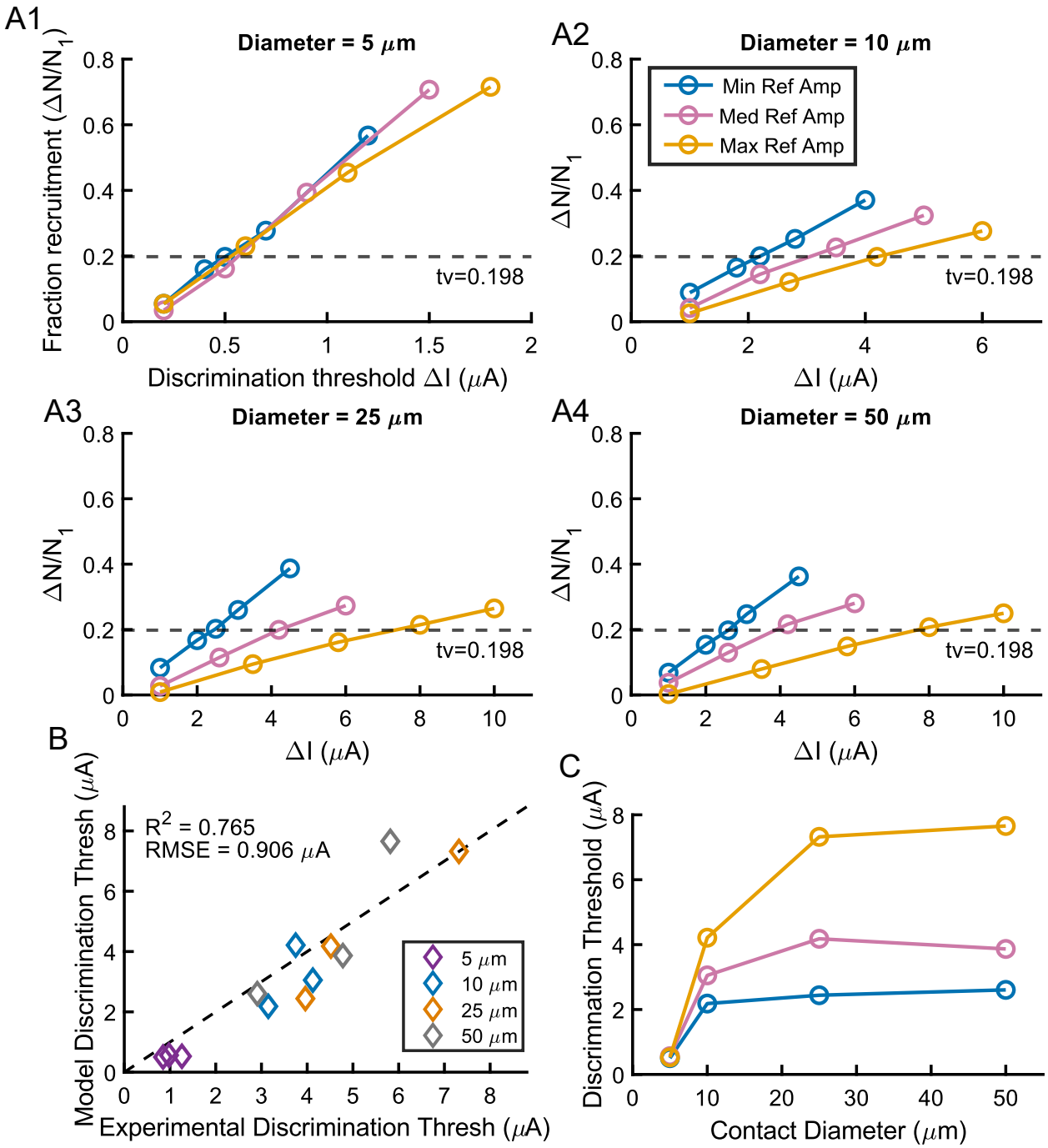


Figure 3: Example of computation of discrimination thresholds in the model at the reference stimulating electrode depth. Fractional change in activation ($\Delta N/N_1$) as a function of the difference in reference and discrimination window intensities (ΔI) at contact diameters of (A1) 5 μm, (A2) 10 μm, (A3) 25 μm, and (A4) 50 μm. The dashed line indicates the neural response threshold value (tv) at which the model-based ΔI yielded the best fit to the experimental ΔI values. The model-based ΔI value corresponding to the $\Delta N/N_1$ tv of 0.198 was determined as the model-based discrimination threshold. (B) Goodness of fit between model-derived and experimentally measured discrimination thresholds across contact diameters. Coefficient of determination (R^2) and root mean square error (RMSE) were computed to assess the quality of fit. (D) Model-based discrimination threshold as a function of contact diameter at three reference amplitude levels.

For each metric of model neuron activation, the discrimination threshold (ΔI) was computed as the difference in stimulation amplitude between the discrimination and reference windows at a given neural response threshold (Fig. 3). We ran simulations across different combinations of reference and discrimination window amplitudes at the reference depth, and using these data, ΔI was derived at a given neural response threshold via linear interpolation (Fig. 3A). Multiple combinations of reference and discrimination window intensities (6-8 discrimination window amplitudes per reference amplitude) were simulated to minimize interpolation-related errors. The optimal neural response threshold (tv) was determined by minimizing the sum of squared errors (SSE) between model-predicted discrimination thresholds at the reference depth and mean experimentally measured discrimination thresholds (averaged across rats) (Fig. S3), pooled across contact diameters and reference amplitudes, using a nonlinear optimization algorithm (fminsearch, MATLAB). The quality of fit between the model and mean experimental discrimination thresholds was assessed using the root mean square error (RMSE) and coefficient of determination, R^2 (Fig. 3B). Model-predicted discrimination thresholds were plotted as a function of contact diameter at the three reference amplitude levels (Fig. 3C). We assessed the sensitivity of stimulation depth on discrimination thresholds derived using the various neural metrics, by computing thresholds at two depths (± 150 μm) from the reference depth. In this case, the optimal neural response threshold for each neural metric was determined by minimizing the SSE between the mean model-predicted discrimination thresholds (averaged across 3 stimulation depths) and the mean experimentally measured discrimination thresholds (averaged across rats). Using this single optimal threshold value, we determined the discrimination thresholds at individual stimulation depths and computed the coefficient of variation (CV = SD/Mean) of model-predicted discrimination thresholds across stimulation depths for each neural metric. We compared the CV of discrimination thresholds across stimulation depths with the CV of discrimination thresholds across rats to see if threshold variability across rats is due to differences in the depth of stimulation across the column. To quantify the sensitivity of stimulation intensity on ICMS-induced perception, we computed the Weber fraction using the equation $\Delta I/I_1$. To study the variation of discrimination threshold and Weber fraction across cortical layers, layer-specific discrimination thresholds and Weber fractions were computed from neural responses in each layer, with the same neural response threshold used to derive discrimination thresholds from activated neurons across all layers.

(4) RESULTS:

(4.1) Experimental Measurements of Discrimination Thresholds:

Six rats were chronically implanted with custom silicon MEA, referred to as ‘G1’, targeting the forepaw region of primary somatosensory cortex (S1), and behavioral testing began five days after surgery. To quantify discrimination thresholds across electrode sizes, we used a single-channel stimulation paradigm in which the discrimination amplitude was adaptively modulated according to the animal’s performance, while all parameters of the reference stimulus (amplitude, frequency, phase duration, polarity, and train duration) remained constant within a session. The just-noticeable difference (JND) was defined as the difference between the reference and discrimination amplitudes that yielded a 50% detection probability. Over 12 weeks of testing, thresholds were obtained for all eight electrode sizes, with both the tested size and the reference amplitude randomized across sessions. In total, 389 thresholds were collected across all (n = 6) animals.

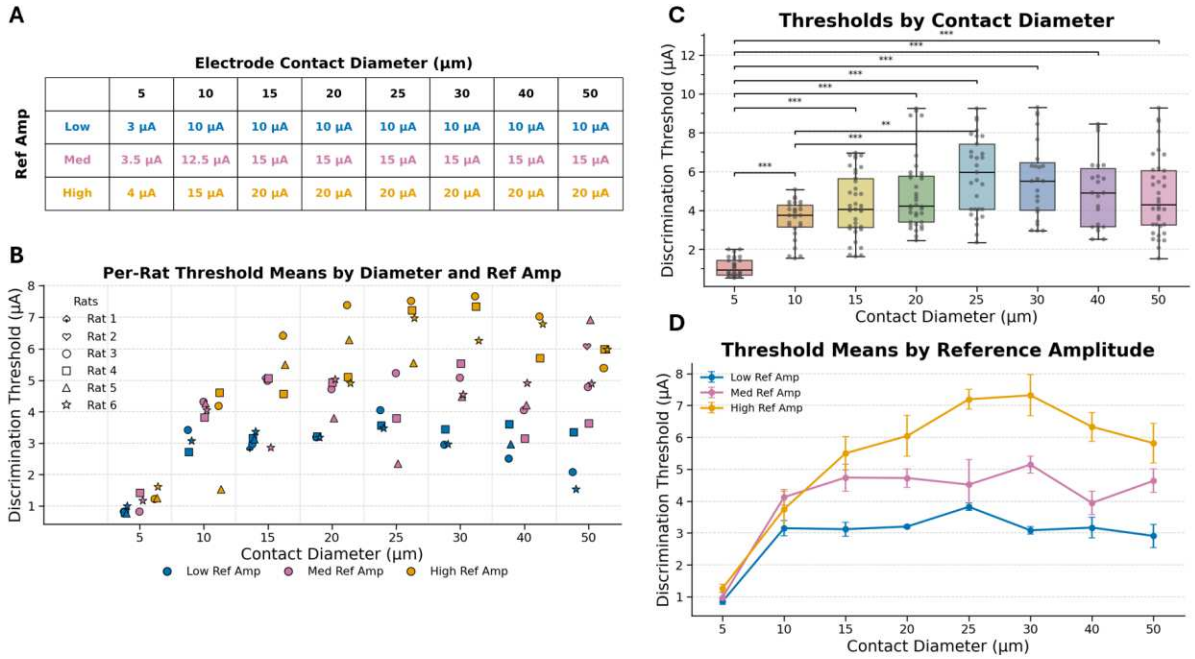


Figure 4: Effects of electrode contact size and reference amplitude on ICMS discrimination thresholds. (A) Table of reference stimulation amplitudes used for each electrode contact diameter (5–50 µm) across low, mid, and high reference amplitude conditions. (B) Per-animal mean discrimination thresholds plotted as a function of electrode diameter and reference amplitude. Each point represents the average threshold for a single rat under a specific diameter–amplitude condition. (C) Distribution of discrimination thresholds across contact diameters. Boxplots show median, interquartile ranges, and individual trial-level measurements lumped across rats and reference amplitudes. Asterisks indicate significant differences across diameter groups (one way ANOVA with diameter and ref amp, and rat as a random factor *p < 0.05, **p < 0.01, ***p < 0.001). (D) Mean discrimination thresholds grouped by reference amplitude condition (low, medium, high).

Each electrode size was evaluated at three reference amplitudes within the recommended charge density limits and effective stimulation range labeled Low, Med, and High (Cogan et al, 2016). For electrode diameters between 15 and 50 µm, these amplitudes were 10, 15, and 20 µA. For the smallest electrodes, amplitudes were reduced accordingly: 3, 3.5, and 4 µA for the 5 µm sites, and 10, 12.5, and 15 µA for the 10 µm sites (Fig. 4A). The full distribution of thresholds is shown in Fig. 4B.

When pooled across rats and reference amplitudes, discrimination thresholds varied with electrode diameter (Fig. 4C; one-way ANOVA: $F(7,229)=21.745$, $p=2.0715e-22$). Tukey-Kramer post-hoc tests showed that 5 µm electrodes had lower thresholds than every larger diameter (5 vs 10 µm: $p=2.43e-6$; 5 vs 15 µm: $p=7.36e-13$; 5 vs 20 µm: $p=1.12e-17$; 5 vs 25 µm: $p<2.2e-16$; 5 vs 30 µm: $p=2.87e-21$; 5 vs 40 µm: $p=9.31e-15$; 5 vs 50 µm: $p=8.05e-17$). Thresholds for 10 µm electrodes were also lower than 25 and 30 µm electrodes ($p=1.48e-5$ and $p=3.93e-4$, respectively). However, this pooled comparison combines measurements collected at different reference amplitudes. To distinguish whether threshold differences were driven by electrode size itself or by the reference amplitudes paired with each size, we fit two adjusted linear mixed-effects models with rat included as a random effect. The first model treated reference amplitude as a categorical Low/Med/High factor and included electrode size as a fixed effect. This model tested whether thresholds differed across the experimental reference-amplitude categories while accounting for repeated measurements within rats. In this model, thresholds increased significantly from Low to Med and High reference-amplitude groups (Med vs. Low: $\beta=1.154$ µA, $SE=0.230$, $z=5.009$, $p=5.47e-7$; High vs. Low: $\beta=2.510$ µA, $SE=0.227$, $z=11.056$, $p=2.04e-28$),

and electrode-size contrasts relative to 5 µm were also significant (all p≤9.56e-18). However, because the Low/Med/High categories did not correspond to the same absolute currents for all electrode sizes, this model could not fully separate size effects from differences in the actual reference amplitudes used. Therefore, we fit a second linear mixed-effects model in which the categorical reference-amplitude group was replaced with absolute reference amplitude in µA. This model tested whether electrode size explained threshold variability after directly accounting for the actual stimulation current. In this model, absolute reference amplitude was a strong predictor of threshold (β=0.308 µA threshold per 1 µA increase in reference amplitude, SE=0.024, z=12.699, p=6.01e-37), whereas electrode size was no longer significant after accounting for absolute reference amplitude (all size contrasts p≥0.115). Thus, the mixed-effects models indicate that the apparent size effect observed when using Low/Med/High categories is largely explained by differences in the absolute reference amplitudes assigned to different electrode sizes.

To further isolate the effect of contact diameter, we then analyzed only the 15-50 µm electrodes, because these sizes had matched absolute amplitudes at every reference level (Low = 10 µA, Med = 15 µA, High = 20 µA). We performed separate one-way ANOVAs at each amplitude stratification, with data pooled across rats within each stratum. Electrode size was not significant at any matched amplitude: 10 µA ($F(5,38)=1.626$, $p=0.1767$), 15 µA ($F(5,60)=0.694$, $p=0.6297$), or 20 µA ($F(5,66)=1.815$, $p=0.1219$), and all within-stratum Tukey-Kramer post-hoc comparisons were nonsignificant. Thus, the lower pooled thresholds observed for 5 and 10 µm contacts are best explained by the lower absolute reference currents used for those electrodes, rather than by an independent effect of contact diameter on discrimination sensitivity at matched current levels.

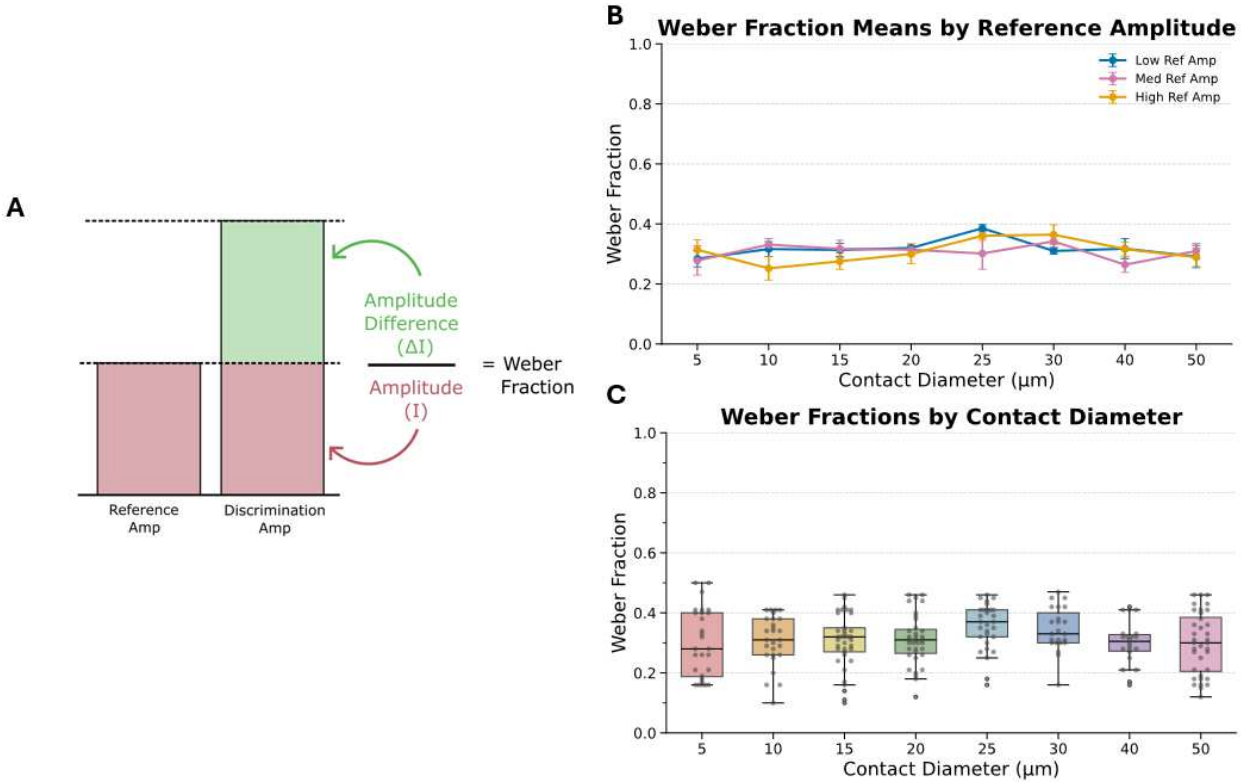


Figure 5: Characterization of Weber fractions across electrode diameters and reference amplitudes.

(A) Illustration of Weber fraction computation. The Weber fraction is defined as the ratio between the amplitude difference required for discrimination (ΔI) and the reference amplitude (I). (B) Mean Weber fractions plotted by reference amplitude (low, mid, high) across electrode contact diameters. Error bars represent standard error of the mean. (C) Distribution of Weber fractions grouped by contact diameter. Boxplots depict median, interquartile ranges, and individual measurements for each diameter condition.

To characterize discrimination sensitivity relative to baseline stimulation, we computed Weber fractions (ΔI/I), defined as the threshold difference normalized by the reference amplitude (Fig. 5A). Weber fractions did not differ significantly across electrode sizes in a pooled one-way ANOVA ($F(7,229)=1.67$, $p=0.1173$, partial $\eta^2 =0.0486$; Fig. 5B), and all Tukey-Kramer post hoc comparisons were nonsignificant. Weber fractions also did not differ across low, mid, and high reference-amplitude groups ($F(2,234)=0.103$, $p=0.9023$, partial $\eta^2 =0.00088$; Fig. 5C), with nonsignificant post hoc comparisons among all reference-amplitude groups. The same pattern held when reference amplitude was treated as absolute current ($F(6,230)=0.485$, $p=0.8194$) and when reference amplitudes were tested within each electrode size (all $p>=0.1330$). Thus, although absolute JNDs increased with reference amplitude, the normalized discrimination threshold remained relatively stable across electrode sizes and stimulation levels, indicating proportional scaling of JND with baseline current over the tested range.

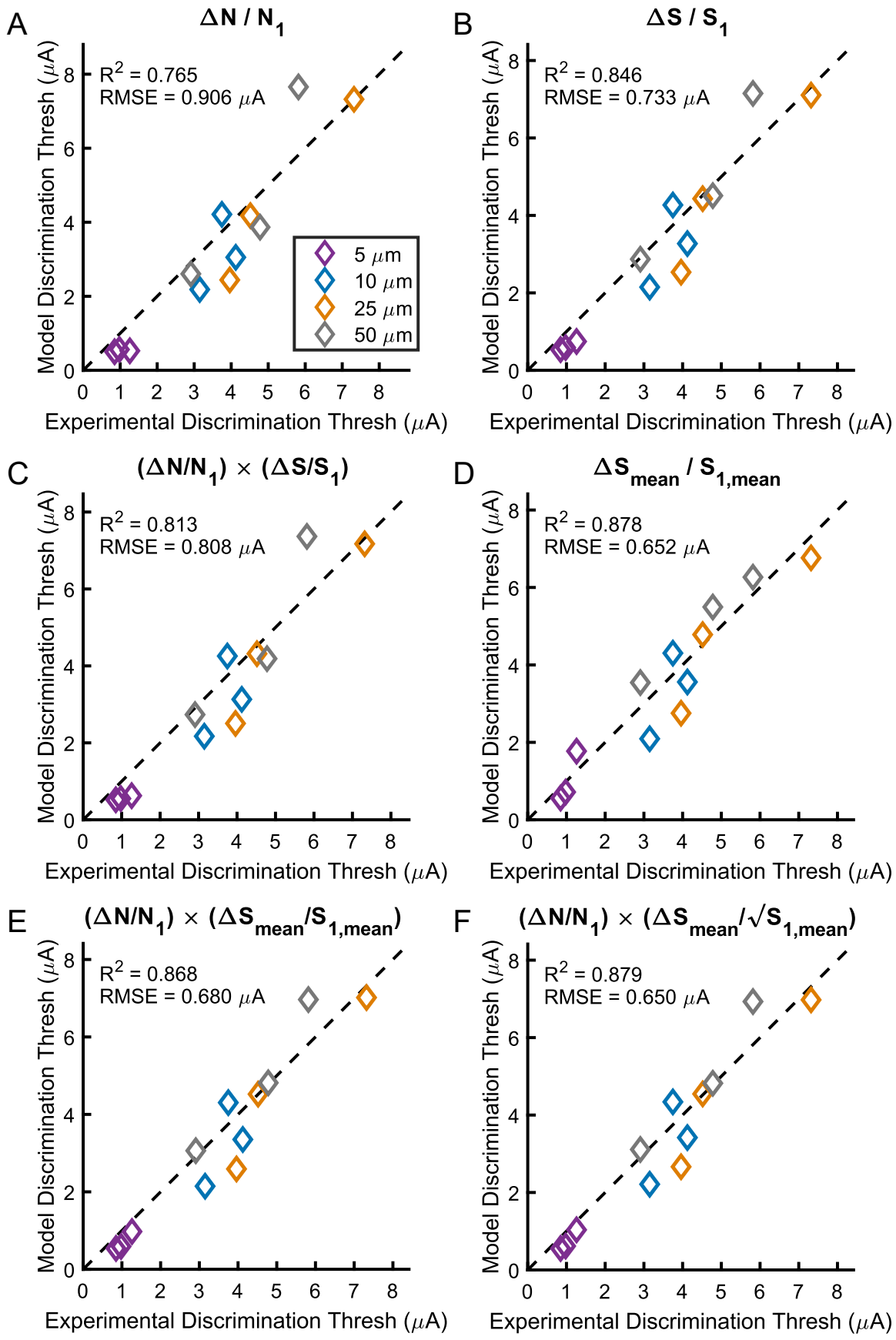

A
ΔN / N1
R2 = 0.765
RMSE = 0.906 μA
5 μm
10 μm
25 μm
50 μm
B
ΔS / S1
R2 = 0.846
RMSE = 0.733 μA
C
(ΔN/N1) × (ΔS/S1)
R2 = 0.813
RMSE = 0.808 μA
D
ΔSmean / S1,mean
R2 = 0.878
RMSE = 0.652 μA
E
(ΔN/N1) × (ΔSmean/S1,mean)
R2 = 0.868
RMSE = 0.680 μA
F
(ΔN/N1) × (ΔSmean/√S1,mean)
R2 = 0.879
RMSE = 0.650 μA
Model Discrimination Thresh (μA)
Experimental Discrimination Thresh (μA)

Figure 6: Model neuron activation correlates of ICMS-induced discrimination threshold in rat S1. Correlation between model-predicted and mean experimentally measured discrimination thresholds with model thresholds derived through (A) fractional change in neural activation ($\Delta N/N_1$), (B) fractional change in spike count ($\Delta S/S_1$), (C) combined fractional changes in neural activation and spike count ($\Delta N/N_1$)*($\Delta S/S_1$), (D) fractional change in population mean spike count ($\Delta S/S_{1,mean}$), (E) combined fractional changes in both neural activation and population mean spike count ($\Delta N/N_1$)*($\Delta S/S_{1,mean}$), (F) combined fractional changes in both neural activation and noise-normalized mean spike count ($\Delta N/N_1$)*($\Delta S/\sqrt{S_{1,mean}}$). The mean experimental discrimination thresholds were averaged across rats. The model discrimination thresholds were derived from the stimulating electrode located at the reference depth. R^2 and RMSE were computed to assess the fit quality.

(4.2) Model-Based Neural Correlates of Discrimination Thresholds:

We quantified model neuron correlates of ICMS-induced perceptual discrimination by computing discrimination thresholds using model-based neural activation metrics classified into three categories: (1) response magnitude-based metrics, (2) population mean-based metrics, and (3) variance-scaled population metrics. Model-derived discrimination thresholds were compared with mean experimentally measured values (averaged across rats), with the unity slope line shown for reference (Fig. 6). Among response magnitude-based metrics, the fractional change in total spike count ($\Delta S/S_1$; R^2 = 0.846, RMSE = 0.733 μA; Fig. 6B) showed a slightly better correlation with experimental discrimination thresholds than the fractional change in neural activation ($\Delta N/N_1$; R^2 = 0.765, RMSE = 0.906 μA; Fig. 6A). The combined metric ($\Delta N/N_1$)*($\Delta S/S_1$) did not improve the correlation compared to $\Delta S/S_1$ alone (R^2 = 0.813, RMSE = 0.808 μA; Fig. 6C). Among population mean-based metrics, the fractional change in mean spike count ($\Delta S/S_{1,mean}$) showed improved correlation with experimental thresholds (R^2 = 0.878, RMSE = 0.652 μA; Fig. 6D). Combining this with activation ($\Delta N/N_1$)*($\Delta S_{mean}/S_{1,mean}$) yielded similar performance (R^2 = 0.868, RMSE = 0.680 μA; Fig. 6E). Although the variance-scaled metric ($\Delta N/N_1$)*($\Delta S_{mean}/\sqrt{S_{1,mean}}$) provided the highest correlation (R^2 = 0.879; Fig. 6F) and lowest error (RMSE = 0.650 μA), the differences in predictive power compared to the response magnitude and population mean-based metrics were subtle. These results suggest that rather than a single metric exhibiting superior performance, multiple representations of model-based neuronal activity perform comparably well at predicting experimental discrimination thresholds.

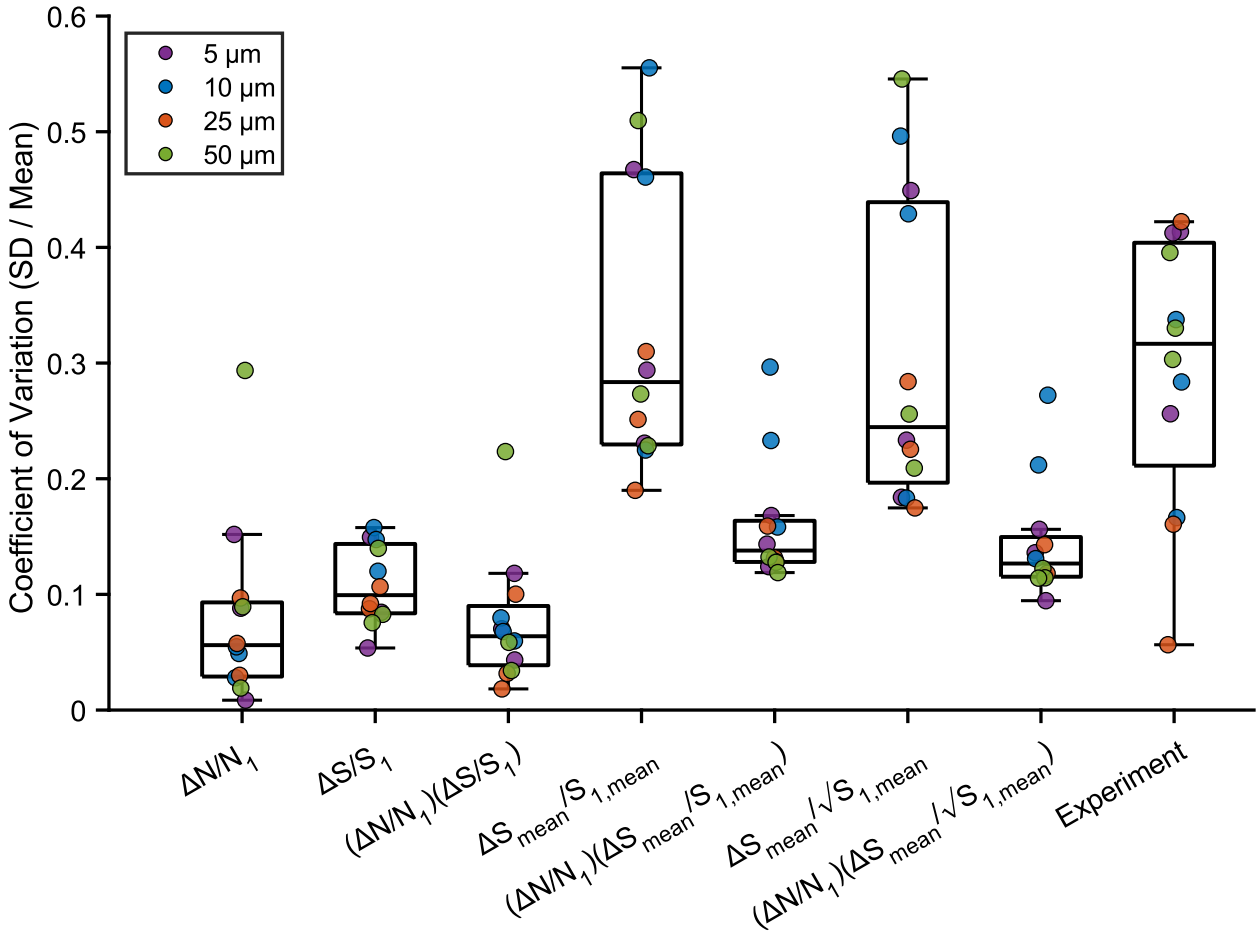


Figure 7: Stimulation depth sensitivity of model-based discrimination thresholds across neural activation metrics. Coefficient of variation (CV) of model-predicted discrimination thresholds across stimulation depths for each neural metric, compared to the CV of experimental discrimination thresholds across rats. Each filled circle on the box (color-coded by contact diameter) represents a stimulation condition (combination of reference amplitude and contact diameter). For each metric, a single neural response threshold value (tv) was used to determine the discrimination threshold across different stimulation depths, and this tv was obtained by minimizing the SSE between the mean model-predicted discrimination thresholds (averaged across depths) and the mean experimental discrimination thresholds (averaged across rats). Please refer to Fig. S4 for the goodness of fit between mean model thresholds and mean experimental thresholds.

To assess the sensitivity of the model-predicted discrimination thresholds to the stimulating electrode depth, we compared the mean model discrimination thresholds (averaged across three depths: the reference depth and two depths at ± 150 µm from the reference depth) with the mean experimental discrimination thresholds averaged across rats (Fig. S4). Mean model discrimination thresholds derived using response magnitude-based metrics exhibited a stronger correlation with mean experimental discrimination thresholds than discrimination thresholds derived using population mean-based metrics (Fig. S4). Further, the CVs of model-based discrimination thresholds across stimulation depths were lower for response magnitude-based metrics than for population mean spike count-based metrics (Fig. 7), indicating the response magnitude-based metrics were less sensitive to changes in stimulation depth. The CVs of population mean-based metrics were more similar to the variability in discrimination thresholds seen in the experimental data across rats (Fig. 7). These results suggest that ICMS-induced perceptual discrimination might not be determined solely by neural response magnitude, i.e., number of activated neurons,

or by population mean spike count, but rather by a combination of both, with response magnitude capturing the mean threshold and average spike count representing the threshold variability.

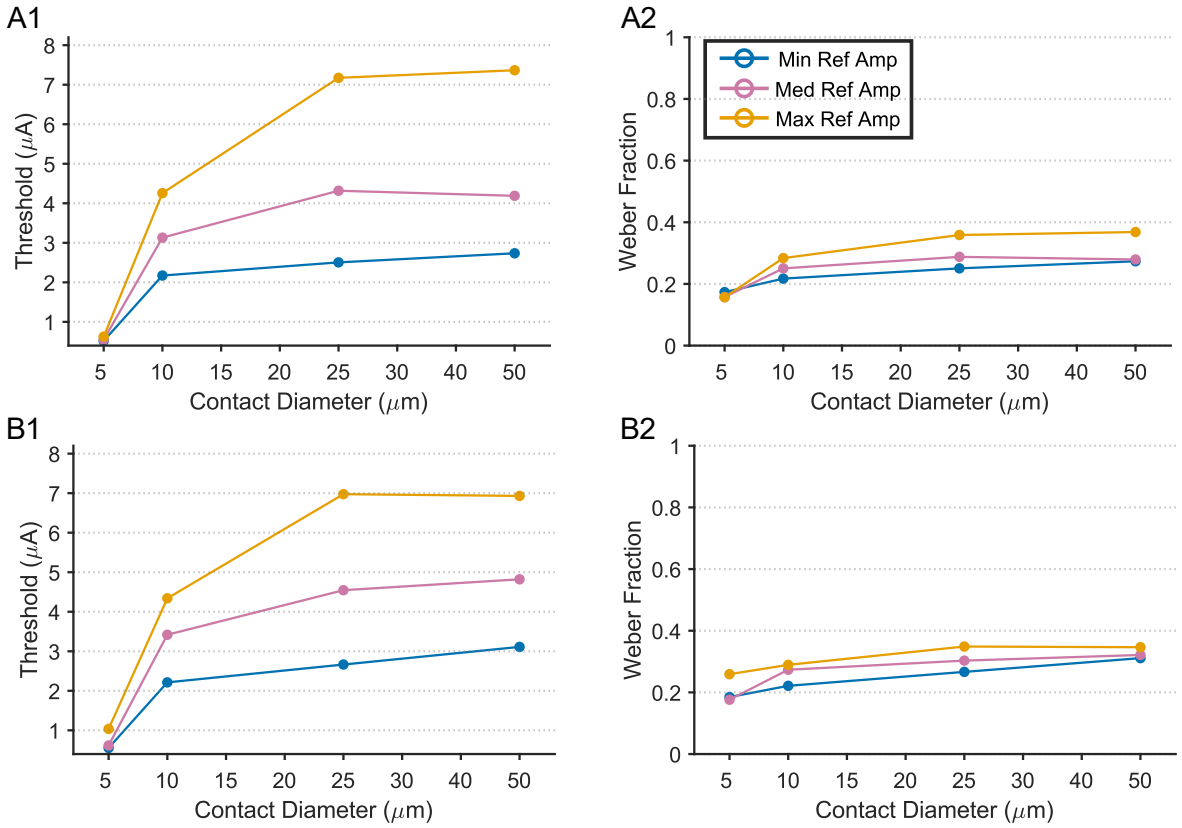


Figure 8: Effect of reference amplitude and contact diameter on discrimination threshold and Weber fraction with model thresholds derived from (A) response magnitude-based neural activation metric $(\Delta N/N_1)$*$(\Delta S/S_1)$. (B) Variance-scaled neural activation metric $(\Delta N/N_1)$*$(\Delta S_{mean}/\sqrt{S_{1,mean}})$. The model discrimination thresholds were derived from the stimulating electrode located at the reference depth.

We plotted discrimination thresholds and Weber fractions as a function of contact diameter at three reference amplitude levels for metrics based on response magnitude $(\Delta N/N_1)$*$(\Delta S/S_1)$ and variance scaling $(\Delta N/N_1)$*$(\Delta S_{mean}/\sqrt{S_{1,mean}})$ (Fig. 8A, B). Model-predicted discrimination thresholds derived from both metrics increased with reference amplitude, consistent with experimental observations (Fig. 8 A1, B1). Discrimination thresholds for the 5 μm contact were considerably lower due to the smaller reference amplitudes (3-4 μA) compared with those for the larger contact diameters (>10 μA). Model-predicted Weber fractions varied little across contact diameters and reference amplitudes, broadly consistent with experimental data, and suggesting adherence to Weber's law over the tested parameter range (Fig. 8 A2, B2). As model determined discrimination thresholds required defining an optimal threshold value, tv, (Fig. 3), we quantified sensitivity to tv, and thediscrimination thresholds were stable to changes in the optimal threshold value across metrics (Fig. S5). To assess layer-specific contributions, we quantified discrimination thresholds and Weber fractions using neural responses within individual cortical layers, and layer-specific discrimination thresholds followed trends similar to the all-layer analyses, varying primarily with reference amplitude rather than contact diameter (Fig. S6, S7). Both discrimination thresholds and Weber fractions were notably larger in L4 and L5 compared to L2/3 and L6, suggesting non-uniform contributions of individual cortical layers to ICMS-induced perceptual

discrimination, with L4 and L5 exhibiting greater sensitivity to changes in stimulation amplitude (Fig. S6, S7). To isolate the effect of contact diameter on the discrimination threshold from that of reference amplitude, we quantified the fractional change in neural metrics while holding the reference amplitude constant across contact diameters (Fig. S8, S9). At fixed stimulation amplitudes, the neural metrics showed no substantial variation across contact diameters in all layers, consistent with the experimental observation that discrimination thresholds are primarily driven by reference amplitude rather than contact diameter (Fig. S8, S9).

(5) DISCUSSION:

(5.1) Electrode size shapes the operating range for ICMS discrimination

Our results show that smaller electrode contacts achieved lower absolute ICMS amplitude discrimination thresholds under the stimulation conditions tested. When thresholds were pooled across reference amplitudes, 5 μm and 10 μm electrodes exhibited significantly smaller discrimination thresholds than larger contacts. This finding is consistent with the expectation that smaller electrodes produce smaller changes in neural activation, measured by the number of activated neurons and/or spikes, for a given change in current amplitude. We define this relationship as stimulation resolution, with smaller changes in neural activation indicating finer resolution.

However, these electrode size-related differences in discrimination thresholds were largely explained by differences in reference amplitudes used to ensure that electrodes operated below established charge safety limits. After controlling for reference amplitude, electrode size no longer contributed to variations in discrimination thresholds, which increased monotonically with reference amplitude across contact diameters. The modeling results show no substantial variation in neural metrics across contact diameters at a fixed reference amplitude, suggesting that contact diameter plays only a minimal role in directly influencing the discrimination thresholds. Weber fractions were also stable across electrode sizes and stimulation conditions, indicating that JNDs scaled proportionally with baseline intensity. This proportional scaling is consistent with classical psychophysical principles and with prior studies of ICMS-evoked perception (Romo et al. 1998; Kim et al. 2015; Bjanes and Moritz 2019; Callier et al. 2019). Together, these findings suggest that miniaturization did not alter the underlying psychophysical scaling rule for amplitude discrimination.

Rather, the benefit of ultra-microelectrodes was expressed through the stimulation range they made accessible. The smallest contacts operated at lower reference amplitudes to ensure that stimulation remained within established charge density limits for non-damaging stimulation (Merrill et al. 2005; Cogan et al. 2016), and within this operating range, proportionally scaled JNDs corresponded to smaller absolute current differences. This distinction is important for neuroprosthetic design: even if perceptual sensitivity follows the same Weber-like rule across electrode geometries, devices that can evoke discriminable percepts at lower currents can support a greater number of distinguishable stimulation levels and enable finer absolute modulation of stimulus amplitude while remaining within safe charge injection bounds.

Taken together, these findings suggest that ultra-microelectrodes do not need to change the fundamental coding rule for ICMS intensity to provide a functional advantage. By supporting low-current stimulation within electrochemical limits, they may reduce charge injection requirements, improve power efficiency, and promote more spatially restricted neural activation, all of which are desirable for chronic, high-resolution sensory feedback. Further, although similar discrimination thresholds may be achieved with both small and large contacts at low reference amplitudes, the ability to fit more 5 μm sites than 50 μm sites within a given cortical area makes

ultra-microelectrodes preferable for neuroprosthetic applications that require improved precision and bandwidth.

(5.2) Neural correlates of ICMS-induced perceptual discrimination:
Several studies quantify the ability of rodents, nonhuman primates, and humans to discriminate between ICMS parameters, such as intensity, frequency, and pulse width, during S1 stimulation (Bjånes & Moritz 2019, Callier et al. 2020, Fridman et al. 2010, Greenspon et al. 2025, Kim et al. 2015a, Kim et al. 2015b, Romo et al. 2000, Romo et al. 1998). However, very few studies investigate the underlying neural basis of perceptual discrimination. This is mainly due to the lack of concurrent recording of neural responses during ICMS in S1. Quantifying the S1 neural response in experimental studies is challenging due to stimulation artifacts in electrical recordings (Butovas & Schwarz 2003). Electrical recordings from the stimulating channel exhibit artifacts extending for at least ~0.7 ms beyond the stimulus pulse, even with specialized artifact-removal hardware (Sombeck et al. 2022). Efforts to build detailed biophysical models of the cortical column have made significant progress in recent years (Billeh et al. 2020, Dura-Bernal et al. 2023, Markram et al. 2015). Neuron models coupled with realistic electric fields generated by electrical stimulation provide a platform for investigating neural responses to different stimulation parameters. Modeling studies have enabled the quantification of the response of cortical neurons near the stimulation electrode (Kumaravelu & Grill 2024), a response that is challenging to characterize experimentally due to stimulation artifacts.

Such computational models of neural stimulation can provide insights into the mechanisms underlying ICMS-induced percepts. A study by Kim and colleagues provided a computational framework for predicting detection and discrimination thresholds to ICMS in S1 of NHP (Kim et al. 2017). They used a probabilistic, phenomenological population model of spiking neurons, and the change in the population mean spike response, normalized by the variance, showed strong correlation with the experimental discrimination thresholds. This result agrees well with our finding that the change in noise-normalized population mean spike count outperformed all other metrics at the reference stimulating electrode depth, although the population mean spike count was highly sensitive to changes in the stimulating electrode depth, and its correlation with experimental discrimination thresholds varied substantially with stimulation depth. Fridman et al. used a population of spiking neurons based on the leaky integrate-and-fire model to predict the neural correlate of ICMS-induced percepts (Fridman et al. 2010). They found that perceived intensity was related to the total spike count across the activated neuronal population. This result is consistent with our finding that the fractional change in the spike count was highly correlated with perceptual discrimination and was more robust to changes in stimulation depth. These studies assumed a specific neural metric to represent perceptual discrimination including the fractional change in spike count or in population mean spike count normalized by the variance. In contrast, we systematically evaluated the performance of multiple neural metrics using a biophysically realistic modeling framework to identify those that are best correlated with both the mean and variance of discrimination thresholds across rats. Our major finding was that the response magnitude-based metrics (such as changes in neural recruitment, spike counts, etc.) best represented the mean discrimination thresholds across rats, whereas the variability in discrimination thresholds was best explained by changes in the population mean spike count as a function of stimulating electrode depth.

The conclusions regarding whether ICMS amplitude discrimination obeys Weber's law are mixed: studies in NHP and humans suggest that ICMS amplitude discrimination violates Weber's law (Greenspon et al. 2025, Kim et al. 2015a), whereas rodent studies indicate that it follows Weber's law (Bjånes & Moritz 2019). Our experimental results in rats suggest ICMS amplitude discrimination obeys Weber's law. The neural response to ICMS is expected to

increase monotonically at lower intensities, up to a threshold beyond which the response becomes nonlinear due to saturation in neural activation, spike-response refractoriness, etc. (Sombeck et al. 2022). This nonlinear relationship between neural response and stimulation intensity would result in $\Delta I/\mathrm{I}$ not being a constant at higher stimulation intensities. This might explain why Weber's law has been reported to be violated in NHPs and humans, given the higher stimulation intensities used in those studies, whereas rodent studies generally employed lower intensities over which the neural response is expected to scale proportionally with stimulation intensity. Our study used lower stimulation intensities (<20 μA) due to smaller contact sizes, and discrimination thresholds derived from model neuron responses at those lower intensities largely obeyed the Weber's law. Kim and colleagues predicted that the nonlinear scaling of neural response and variance with stimulation intensity would lead to a violation of Weber's law □□(Kim et al. 2017)□; however, they tested only higher stimulation intensities (≥ 20 μA). Thus, our results suggest that Weber's law would hold within the low-intensity operating regime used in this study, whereas deviations from Weber's law might emerge at higher stimulation intensities where scaling of neural responses with stimulation intensity becomes increasingly nonlinear.

(5.3) Experimental Limitations:

Several limitations should be considered when interpreting the findings of the present study. First, stimulation amplitudes were not matched across all electrode sizes due to constraints imposed by charge density limits. Smaller electrodes required lower current amplitudes to remain within established operating bounds, while larger electrodes were tested at higher amplitudes. Although this constraint reflects realistic conditions for implanted devices, it introduced a confounding relationship between electrode size and stimulation amplitude. While our stratified analyses mitigated this issue and allowed isolation of geometric effects, a fully balanced design with identical amplitude ranges across all electrode sizes would provide a more direct comparison.

Second, all experiments were conducted using single-channel stimulation. While this approach enables controlled investigation of amplitude discrimination at individual electrode sites, it does not capture the interactions that arise during multi-channel stimulation, which is commonly employed in neuroprosthetic systems to generate more complex and naturalistic percepts (Greenspon et al. 2025; Bjanes et al. 2025). In multi-electrode paradigms, spatial summation, overlap in neural recruitment, and temporal coordination across channels can substantially alter the resulting percept. These interactions may influence both the magnitude and discriminability of evoked sensations, suggesting that the scaling relationships observed here may differ under multi-site stimulation conditions. Future studies incorporating multi-channel ICMS will be necessary to determine how these effects generalize to more clinically relevant stimulation strategies.

(5.4) Model Limitations:

Although our biophysically realistic modeling framework is the most advanced for studying the neural correlates of ICMS-induced perception, it has some important limitations. First, the model lacked connectivity between neurons and thereby could not account for the contribution of network effects to perception evoked by ICMS. Despite the absence of network effects, the model's neural responses correlated strongly with the experimental discrimination thresholds, indicating that the direct effect of stimulation on a population of neurons might play a more prominent role in mediating ICMS-induced perception. Also, the main goal of this study was to identify neural correlates of ICMS-induced percepts, not to establish a causal link between neural responses and perception, in which indirect network effects might play a more significant role. Second, while our model is deterministic (i.e., no stochastic neural noise), differences in

extracellular drive experienced by each neuron due to spatial heterogeneity in neuron locations within the column, as well as diverse cell types, resulted in variability in spike counts across the activated population. Although the model neurons included detailed morphology comprising soma, dendrite, and axon compartments, neural metrics were computed only from spike counts of activated somata. This is because cell bodies are thought to play a pivotal role in mediating perceptual discrimination. Third, we used amplitude discrimination thresholds at different contact sizes to identify neural correlates but did not vary stimulation parameters such as frequency and pulse width. Although other studies identified neural correlates of perceptual discrimination by varying stimulation intensity, frequency, and pulse width, they did not alter the contact sizes (Fridman et al. 2010, Kim et al. 2017). Our neural correlate results, derived from amplitude discrimination thresholds across contact sizes, are expected to generalize well to discrimination of other stimulation parameters, such as frequency and pulse width. Finally, we assumed the variability in discrimination thresholds seen across rats was due to the differences in stimulating electrode depth within the column. However, this might not be the only source of variability, and additional factors such as differences in training, encapsulation tissue, and brain anatomy might also have contributed to the variability observed across rats.

(6) CONCLUSION:

Our experimental results show that ICMS amplitude discrimination scales proportionally across electrode sizes, with thresholds primarily determined by reference stimulation intensity. The 5 μm and 10 μm contacts produced the lowest absolute discrimination thresholds because they operated at substantially lower reference amplitudes, demonstrating a practical advantage of ultra-microelectrodes for supporting a greater number of distinguishable stimulation levels within their safe operating range. These findings support the use of smaller contacts in sensory feedback systems where low-current activation, high-density stimulation, and non-damaging chronic operation are important design goals.

These experimental findings are supported by our computational results, which provide a mechanistic framework for identifying neural correlates of ICMS-evoked amplitude discrimination across electrode contact sizes. Response magnitude, such as neural recruitment and spike count, strongly correlated with the mean discrimination threshold across rats. The change in the population mean spike count with stimulation depth partially accounted for the variability in discrimination thresholds observed across rats. The model-based neural metrics did not vary substantially with contact diameter at a fixed reference amplitude, further supporting the experimental finding that discrimination thresholds are primarily influenced by reference stimulation amplitude rather than contact diameter. These results help clarify how ICMS parameters shape perception, thereby enabling the optimization of stimulation paradigms for neuroprosthetic applications such as sensory feedback.

(7) ACKNOWLEDGMENTS:

This material is based upon work supported by the National Institutes of Health under Grant NIH 1U01NS126052-01 “Engineering the neuronal response to electrical microstimulation” and the National Science Foundation Graduate Research Fellowship Program under Grant NGE-244108. Any opinions, findings, and conclusions or recommendations expressed in this material are those of the author(s) and do not necessarily reflect the views of the National Institutes of Health or National Science Foundation.

(8) AUTHOR CONTRIBUTIONS:

E.S., V.R., K.K., W.M.G. and K.O. conception and design of research; E.S. and S.S. performed experimental data collection. V.R. and K.K. implemented the computational model; E.S., V.R. and K.K. analyzed data; E.S., V.R., K.K., W.M.G. and K.O. interpreted results; E.S., V.R. and

K.K. prepared figures and drafted manuscript; E.S., V.R., K.K., S.S., W.M.G. and K.O. edited and revised the manuscript; E.S., V.R., K.K., S.S., W.M.G. and K.O. approved the final version of the manuscript.

(9) ADDITIONAL INFORMATION:

The authors declare that they have no conflict of interest.

(10) FUNDING STATEMENT:

This material is based upon work supported by the National Institutes of Health under Grant NIH 1U01NS126052-01 “Engineering the neuronal response to electrical microstimulation” and the National Science Foundation Graduate Research Fellowship Program under Grant NGE-244108.

(11) DATA AVAILABILITY:

The dataset used and/or analyzed during the current study is available from the corresponding author on reasonable request

(12) SUPPLEMENTARY SECTION:

TABLES

Table S1: Layer-specific anisotropic conductivity (σ_r: radial direction, σ_t: tangential direction) used in the finite element model based on measurements from rat S1 (*Goto et al. 2010)

Cortical Lamina	**Layer 2/3**		**Layer 4**		**Layer 5**		**Layer 6**	
Conductivity*								
Mean	3.19	2.31	3.25	2.40	3.53	2.28	2.94	2.68

FIGURES

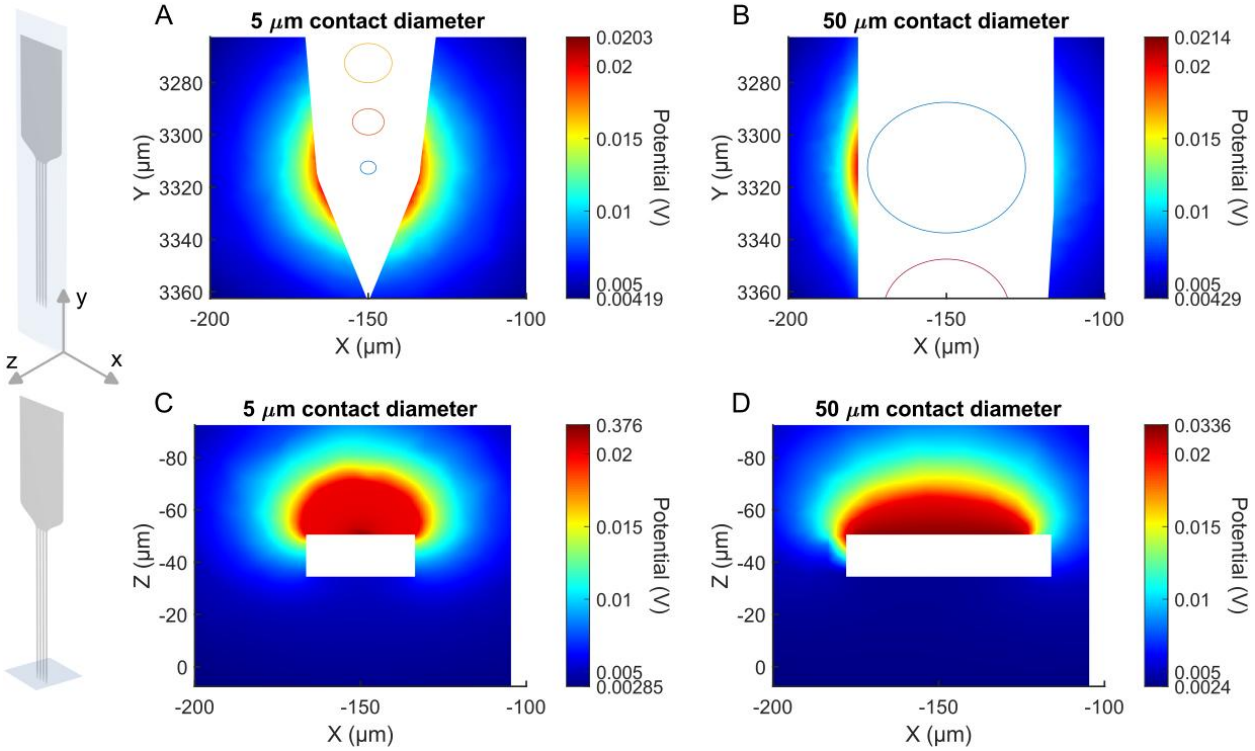


Figure S1: Electric potential generated in the tissue computed using finite element modeling (FEM) of G1 microelectrode array (MEA) at different contact sizes. Potential distribution in the XY plane to 1 μA ICMS delivered through contact sizes of (A) 5 μm, (B) 50 μm. Potential distribution in the XZ plane to 1 μA ICMS delivered through contact sizes of (C) 5 μm, (D) 50 μm.

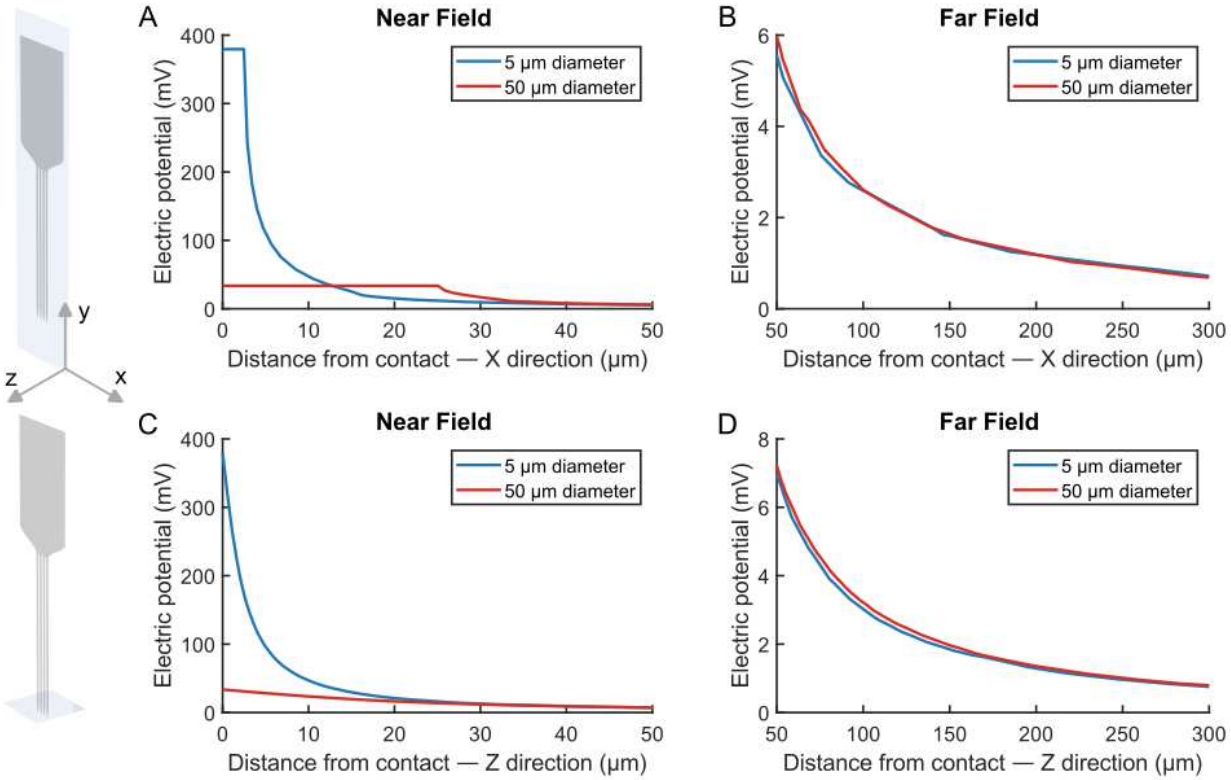


Figure S2: Electric potential generated in the tissue computed using FEM of G1 MEA at different contact sizes. Electric potential plotted as a function of distance from the contact center along the X (lateral) and Z (normal) directions. (A) Near-field potential along the X direction, (B) far-field potential along the X direction, (C) near-field potential along the Z direction, (D) far-field potential along the Z direction. The near-field potential strongly depends on the contact diameter, whereas the far-field potential is largely independent of contact size and approximates that of a point source.

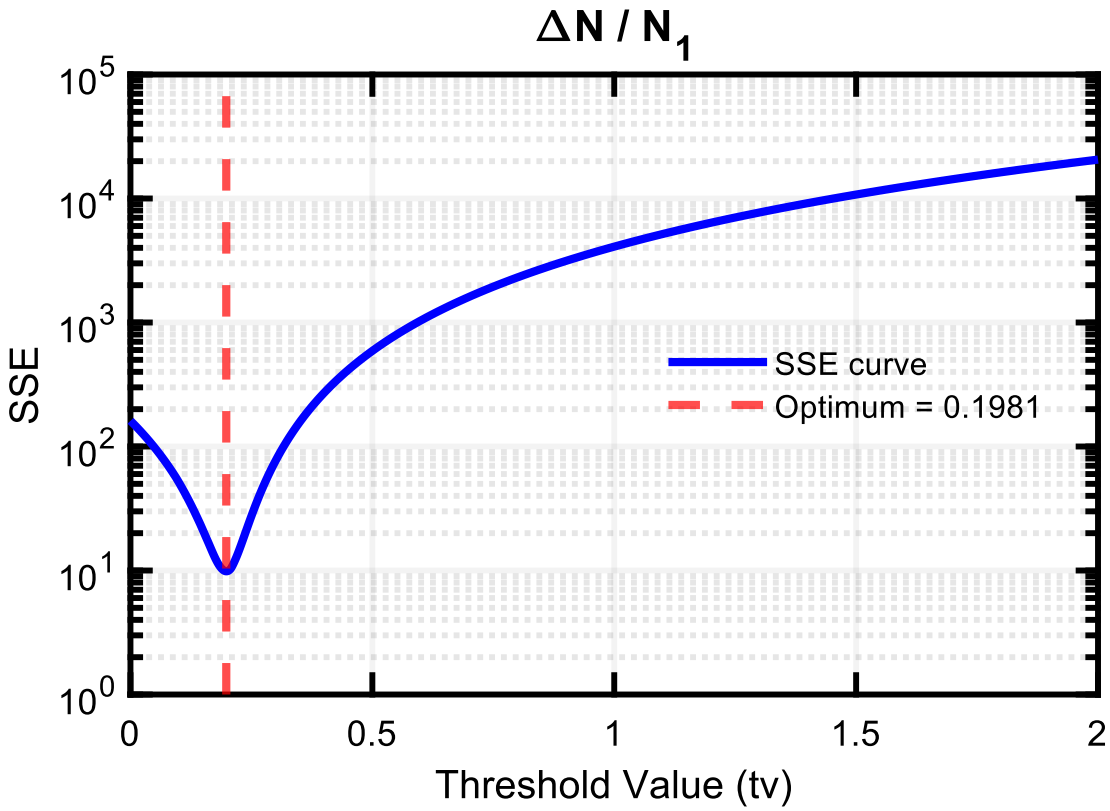


Figure S3: Sensitivity of the threshold value (tv) to the sum of squared error (SSE) for the neural metric ($\Delta N/N_1$). The SSE was minimized at the optimal threshold value (tv = 0.1981) used to determine the model-based discrimination threshold.

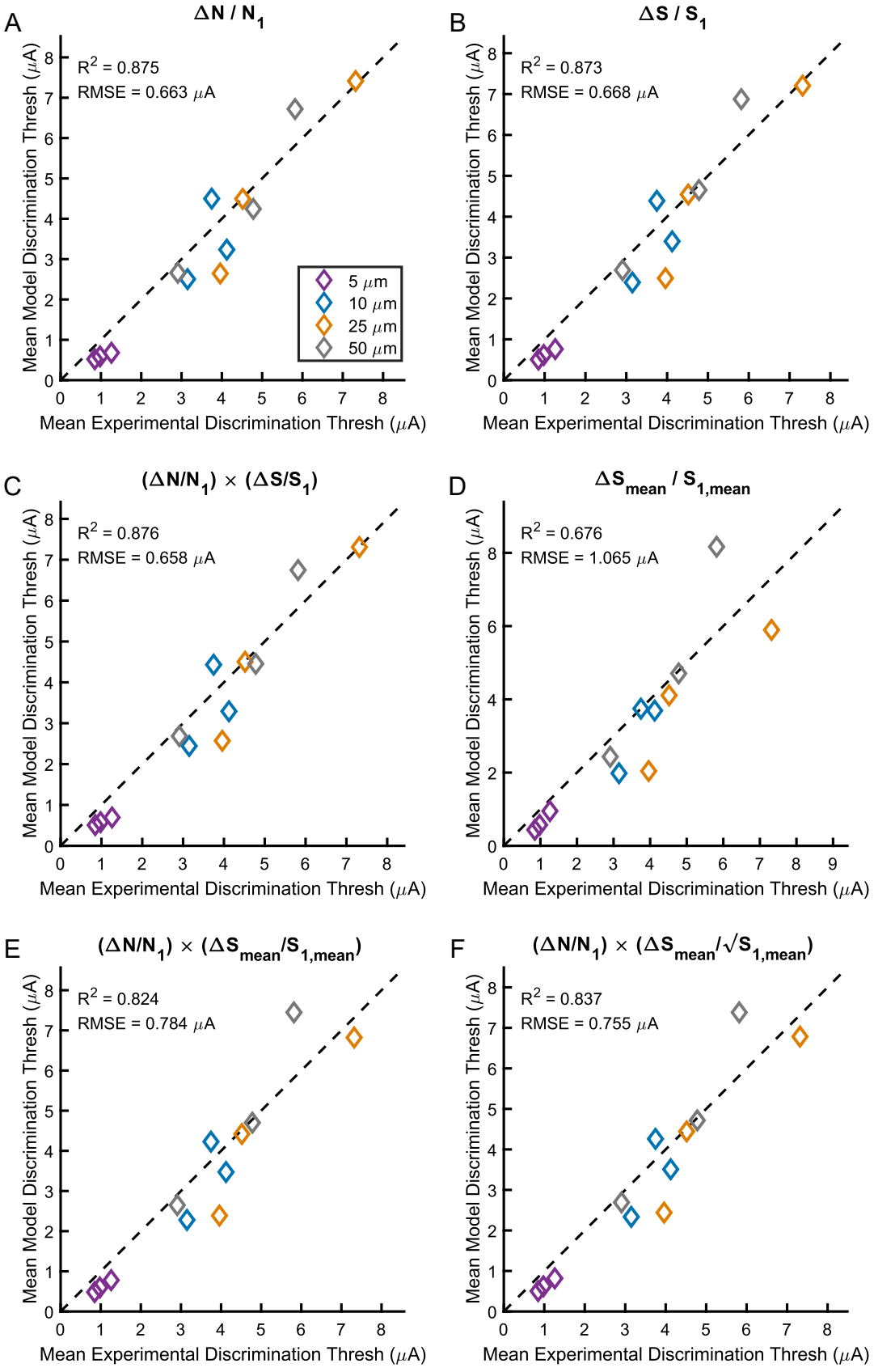

A
ΔN / N1
R2 = 0.875
RMSE = 0.663 μA
5 μm
10 μm
25 μm
50 μm
B
ΔS / S1
R2 = 0.873
RMSE = 0.668 μA
C
(ΔN/N1) × (ΔS/S1)
R2 = 0.876
RMSE = 0.658 μA
D
ΔSmean / S1,mean
R2 = 0.676
RMSE = 1.065 μA
E
(ΔN/N1) × (ΔSmean/S1,mean)
R2 = 0.824
RMSE = 0.784 μA
F
(ΔN/N1) × (ΔSmean/√S1,mean)
R2 = 0.837
RMSE = 0.755 μA
Mean Model Discrimination Thresh (μA)
Mean Experimental Discrimination Thresh (μA)

Figure S4: Goodness of fit between model-predicted discrimination thresholds and experimentally measured discrimination thresholds. Correlation between mean model-predicted discrimination thresholds (averaged across stimulation depths) and mean experimentally measured discrimination thresholds (averaged across rats) for different neural metrics: (A) fractional change in neural recruitment ($\Delta N/N_1$), (B) fractional change in spike count ($\Delta S/S_1$), (C) combined fractional changes in neural recruitment and spike count ($\Delta N/N_1$)*($\Delta S/S_1$), (D) fractional change in population mean spike count ($\Delta S_{mean}/S_{1,mean}$), (E) combined fractional changes in neural recruitment and population mean spike count ($\Delta N/N_1$)*($\Delta S_{mean}/S_{1,mean}$), (F) combined fractional changes in neural recruitment and noise-normalized mean spike count ($\Delta N/N_1$)*($\Delta S_{mean}/\sqrt{S_{1,mean}}$). For each neural metric, a single neural response threshold value (tv) was used to determine discrimination thresholds across all stimulation depths. The optimal tv for each neural metric was obtained by minimizing the SSE between mean model-predicted discrimination thresholds (averaged across depths) and mean experimental discrimination thresholds (averaged across rats).

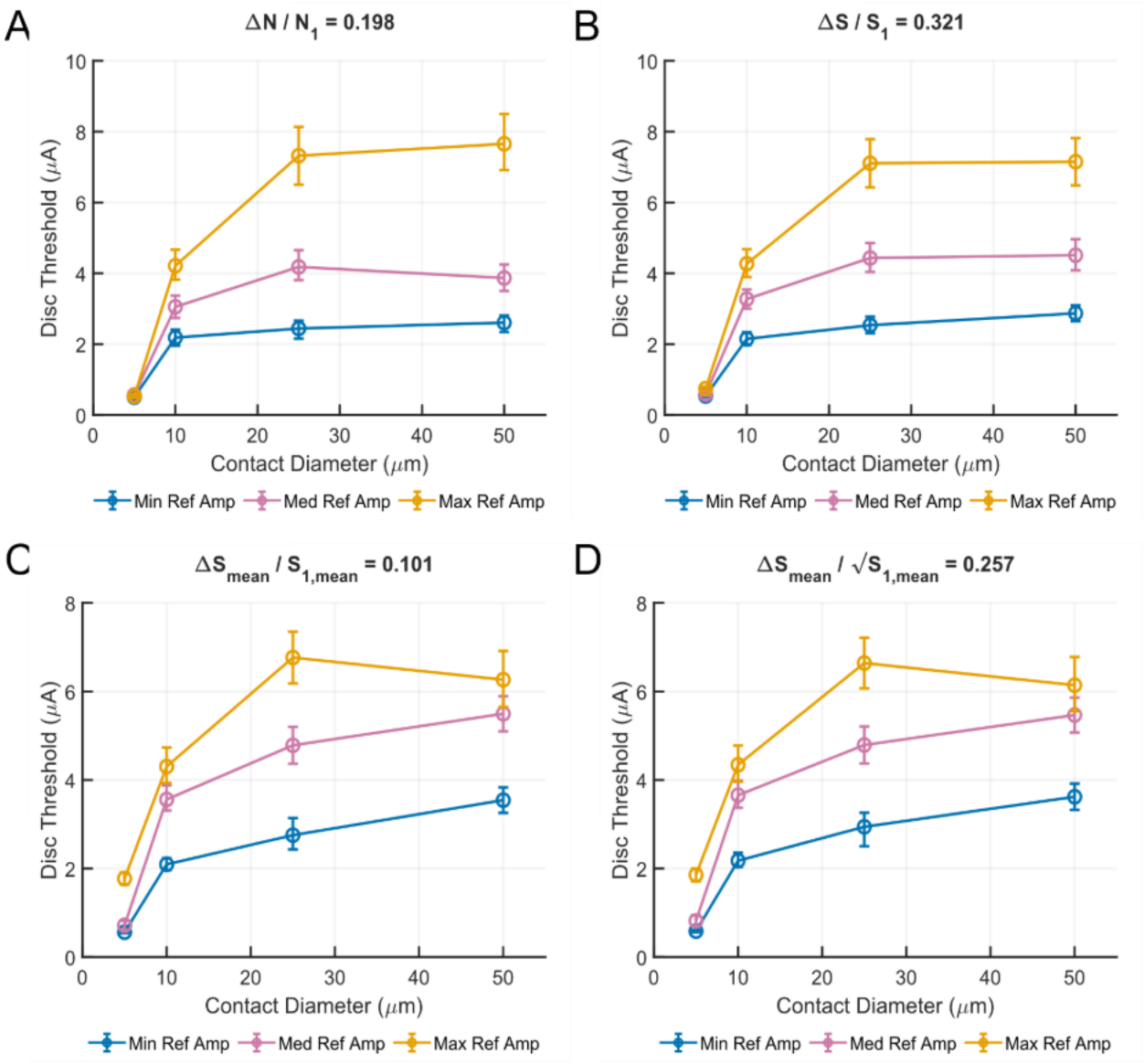


Figure S5: Sensitivity of the threshold value (tv) to the sum of squared error (SSE) for the neural metric ($\Delta N/N_1$). The SSE was minimized at the optimal threshold value (tv = 0.1981) used to determine the model-based discrimination threshold.

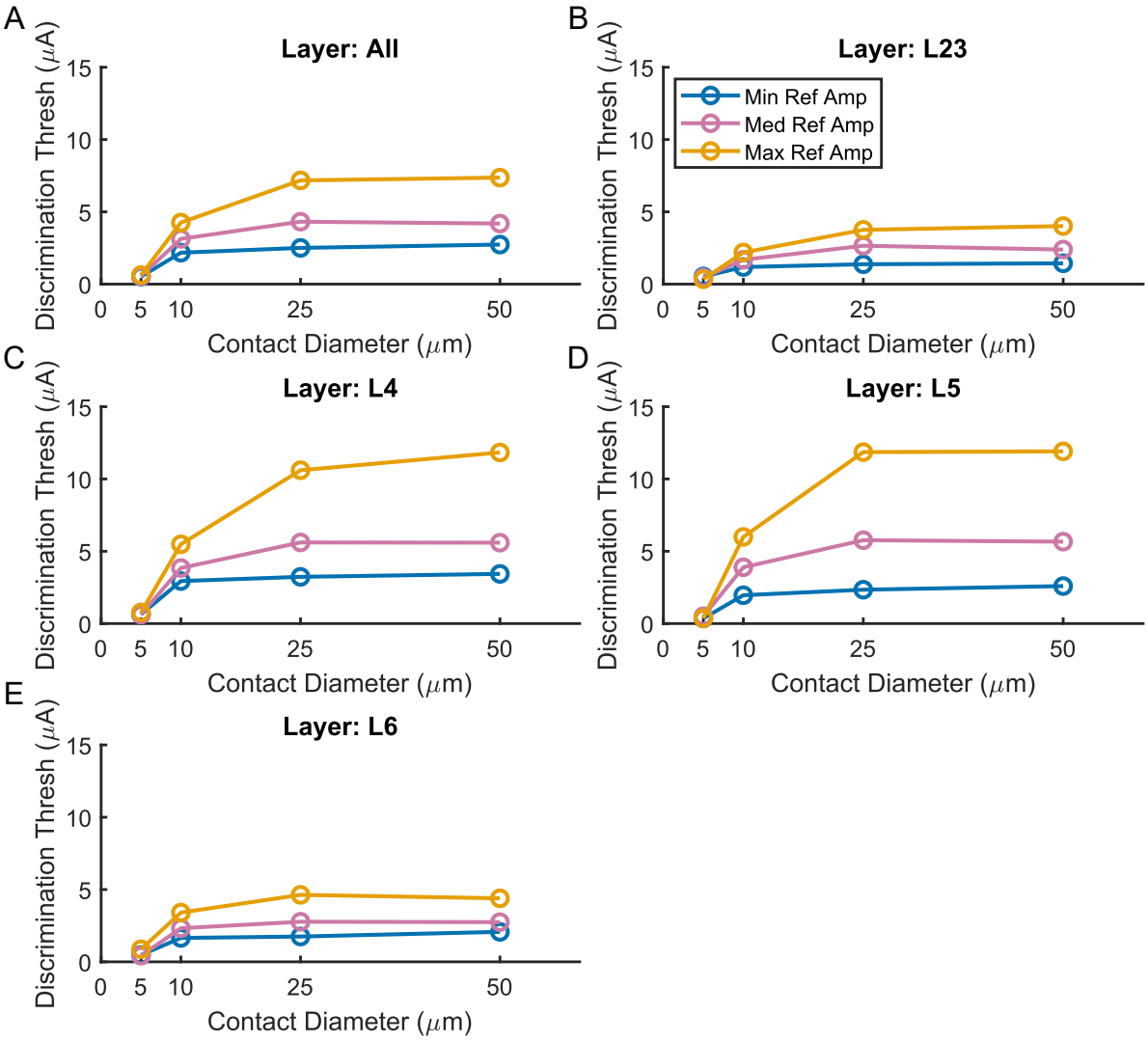


Figure S6: Layer-specific discrimination thresholds predicted by the model. Discrimination thresholds were computed using the combined response magnitude metric $(\Delta N/N_1)$*$(\Delta S/S_1)$ based on neural responses from (A) all layers within the cortical column, (B) L2/3, (C) L4, (D) L5 and (E) L6. The model discrimination thresholds were derived from the stimulating electrode located at the reference depth.

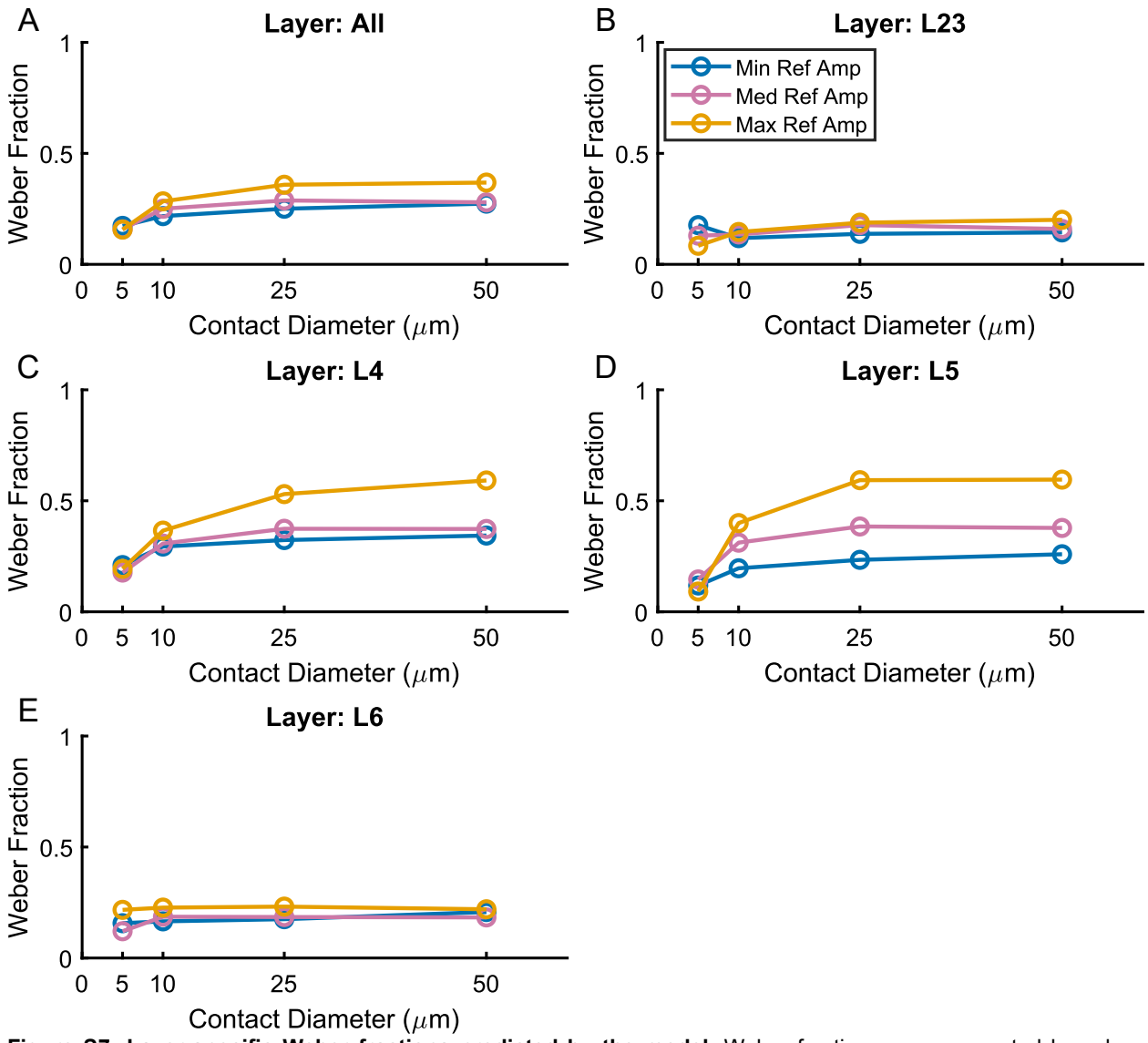


Figure S7: Layer-specific Weber fractions predicted by the model. Weber fractions were computed based on discrimination thresholds from (A) all layers within the column, (B) L2/3, (C) L4, (D) L5 and (E) L6. The discrimination thresholds were derived using the combined response magnitude metric $(\Delta N/N_1)$*$(\Delta S/S_1)$ shown in Fig. S6. The model discrimination thresholds were derived from the stimulating electrode located at the reference depth.

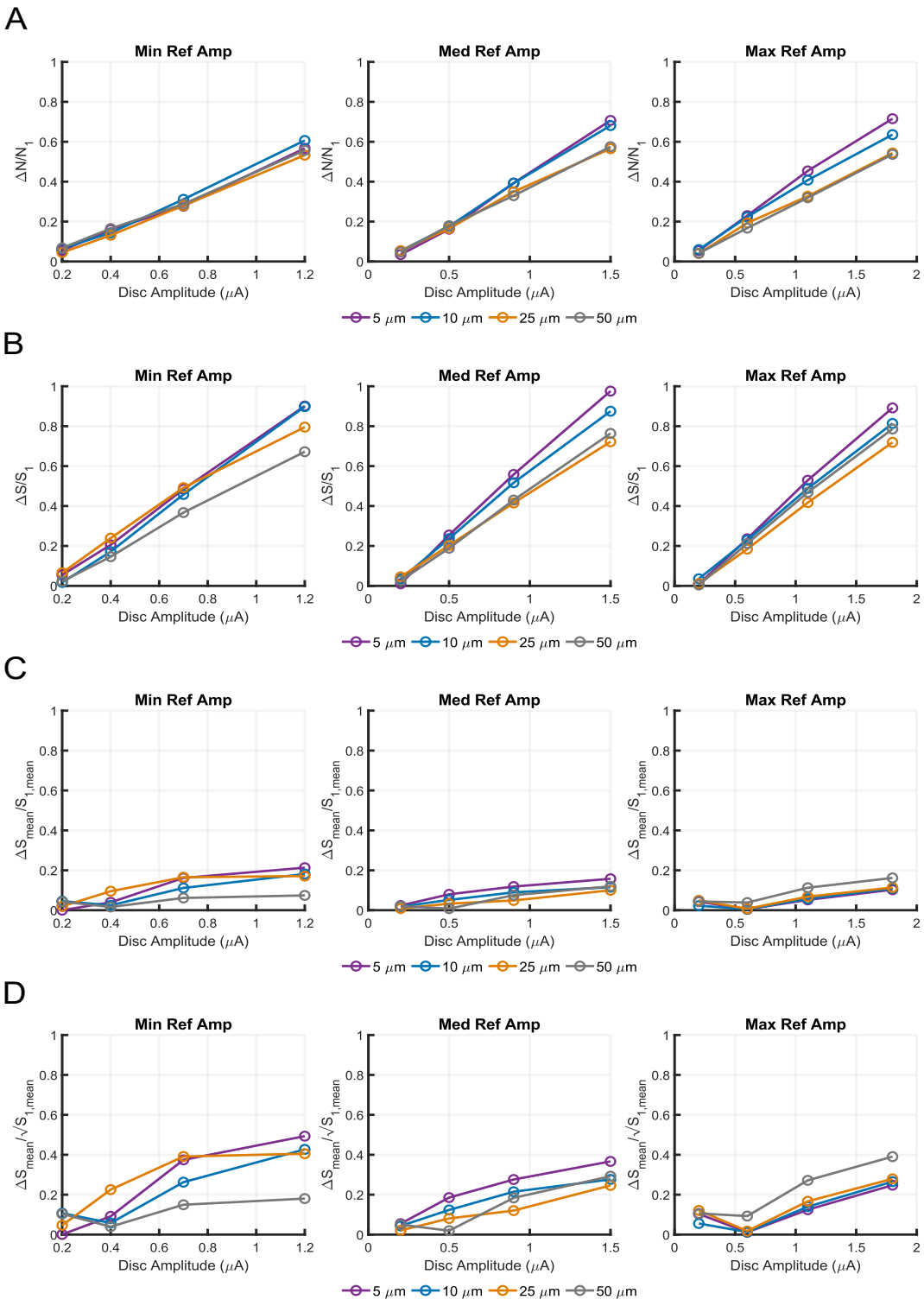


Figure S8: Neural metrics compared across diameters at low reference amplitude values. (A) Fractional change in recruitment ($\Delta N/N_1$), B) fractional change in spike count ($\Delta S/S_1$), C) fractional change in population mean spike count ($\Delta S_{mean}/S_{1,mean}$), D) fractional change in noise-normalized mean spike count ($\Delta N/N_1$)*($\Delta S_{mean}/\sqrt{S_{1,mean}}$) as a function of the difference in reference and discrimination window intensities (ΔI) for reference amplitudes Min Ref Amp: 3 μA, Med Ref Amp: 3.5 μA, Max Ref Amp: 4 μA.

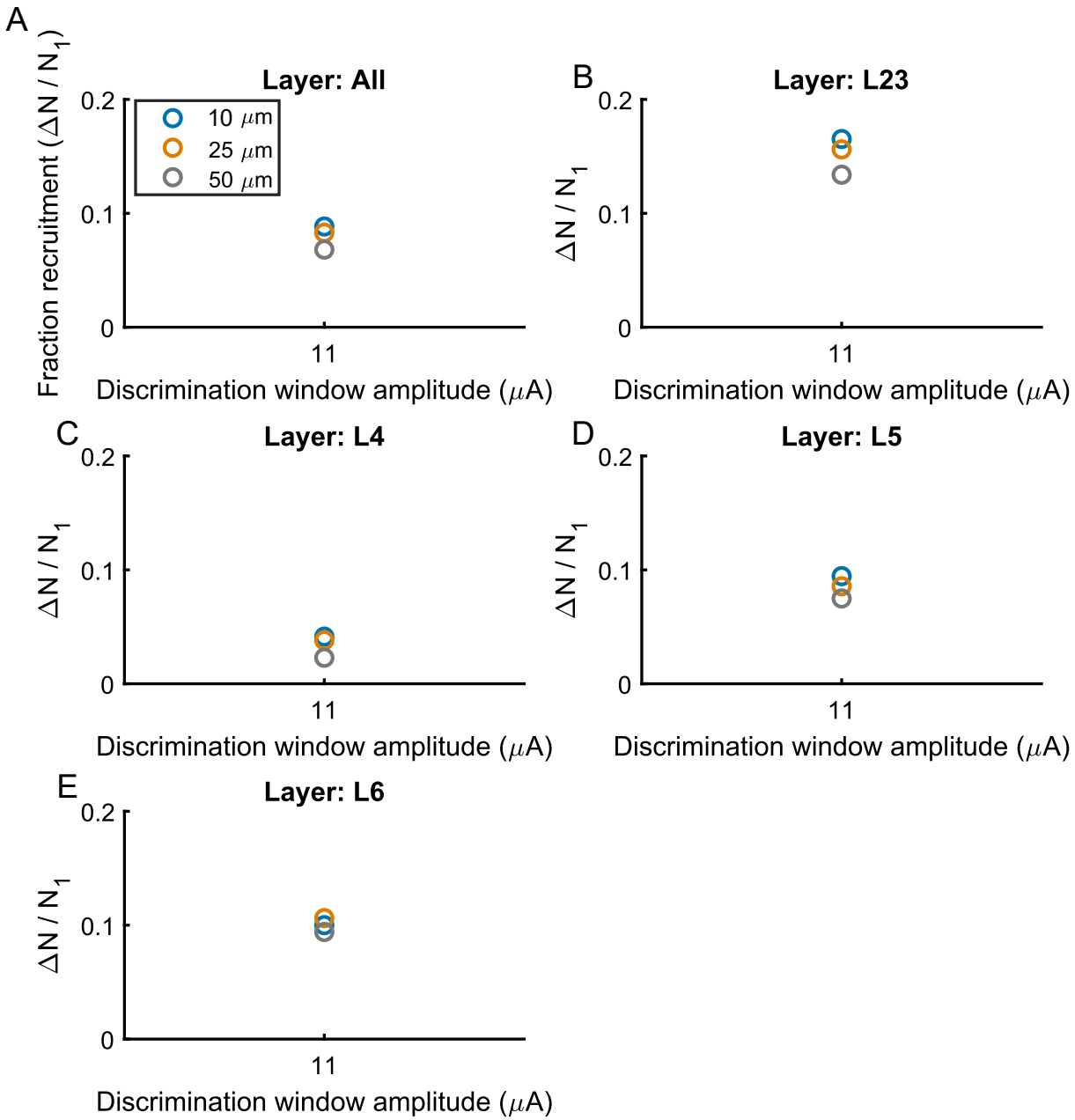


Figure S9: Effect of contact diameter on the fractional change in neural recruitment ($\Delta N/N_1$) at fixed reference (10 µA) and discrimination (11 µA) intensities across contact diameters. ($\Delta N/N_1$) was computed based on neural responses from (A) all layers, (B) L2/3, (C) L4, (D) L5 and (E) L6. At fixed reference window intensity and ΔI, $\Delta N/N_1$ showed minimal variation across contact diameters. The model discrimination thresholds were derived from the stimulating electrode located at the reference depth.

(12) REFERENCES:

Armenta Salas M, Bashford L, Kellis S, Jafari M, Jo H, et al. 2018. Proprioceptive and cutaneous sensations in humans elicited by intracortical microstimulation. eLife 7: e32904

Bensmaia SJ, Miller LE. 2014. Restoring sensorimotor function through intracortical interfaces: progress and looming challenges. Nature Reviews Neuroscience 15: 313-325

Billeh YN, Cai B, Gratiy SL, Dai K, Iyer R, et al. 2020. Systematic integration of structural and functional data into multi-scale models of mouse primary visual cortex. Neuron 106: 388-403.e18

Bjånes DA, Bashford L, Pejsa K, Lee B, Liu CY, Andersen RA. 2025. Charge density of multi-channel intra-cortical micro-stimulation modulates intensity and naturalness of evoked somatosensations. Journal of Neural Engineering 22: 066025

Bjånes DA, Moritz CT. 2019. A robust encoding scheme for delivering artificial sensory information via direct brain stimulation. IEEE Transactions on Neural Systems and Rehabilitation Engineering 27: 1994-2004

Bossetti CA, Birdno MJ, Grill WM. 2008. Analysis of the quasi-static approximation for calculating potentials generated by neural stimulation. Journal of Neural Engineering 5: 44-53

Butovas S, Schwarz C. 2003. Spatiotemporal effects of microstimulation in rat neocortex: a parametric study using multielectrode recordings. Journal of Neurophysiology 90: 3024-3039

Callier T, Brantly NW, Caravelli A, Bensmaia SJ. 2020. The frequency of cortical microstimulation shapes artificial touch. Proceedings of the National Academy of Sciences 117: 1191-1200

Cogan SF, Ludwig KA, Welle CG, Takmakov P. 2016. Tissue damage thresholds during therapeutic electrical stimulation. Journal of Neural Engineering 13: 021001

Cogan SF. 2008. Neural stimulation and recording electrodes. Annual Review of Biomedical Engineering 10: 275-309

Dura-Bernal S, Neymotin SA, Suter BA, Dacre J, Moreira JVS, et al. 2023. Multiscale model of primary motor cortex circuits predicts in vivo cell-type-specific, behavioral state-dependent dynamics. Cell Reports 42: 112574

Flesher SN, Collinger JL, Foldes ST, Weiss JM, Downey JE, et al. 2016. Intracortical microstimulation of human somatosensory cortex. Science Translational Medicine 8: 361ra141

Fridman GY, Blair HT, Blaisdell AP, Judy JW. 2010. Perceived intensity of somatosensory cortical electrical stimulation. Experimental Brain Research 203: 499-515

George JA, Kluger DT, Davis TS, Wendelken SM, Okorokova EV, et al. 2019. Biomimetic sensory feedback through peripheral nerve stimulation improves dexterous use of a bionic hand. Science Robotics 4: eaax2352

Goto T, Hatanaka R, Ogawa T, Sumiyoshi A, Riera J, Kawashima R. 2010. An evaluation of the conductivity profile in the somatosensory barrel cortex of Wistar rats. Journal of Neurophysiology 104: 3388-3412

Greenspon CM, Valle G, Shelchkova ND, Hobbs TG, Verbaarschot C, et al. 2025. Evoking stable and precise tactile sensations via multi-electrode intracortical microstimulation of the somatosensory cortex. Nature Biomedical Engineering 9: 935-951

Histed, M.H., Bonin, V. and Reid, R.C., 2009. Direct activation of sparse, distributed populations of cortical neurons by electrical microstimulation. *Neuron*, *63*(4), pp.508-522.

Johansson RS, Flanagan JR. 2009. Coding and use of tactile signals from the fingertips in object manipulation tasks. Nature Reviews Neuroscience 10: 345-359

Kim S, Callier T, Bensmaia SJ. 2017. A computational model that predicts behavioral sensitivity to intracortical microstimulation. Journal of Neural Engineering 14: 016012

Kim S, Callier T, Tabot GA, Gaunt RA, Tenore FV, Bensmaia SJ. 2015a. Behavioral assessment of sensitivity to intracortical microstimulation of primate somatosensory cortex. Proceedings of the National Academy of Sciences 112: 15202-15207

Kim S, Callier T, Tabot GA, Tenore FV, Bensmaia SJ. 2015b. Sensitivity to microstimulation of somatosensory cortex distributed over multiple electrodes. Frontiers in Systems Neuroscience 9: 47

Koivuniemi AS, Regele OB, Brenner JH, Otto KJ. 2011. Rat behavioral model for high-throughput parametric studies of intracortical microstimulation. 2011 Annual International Conference of the IEEE Engineering in Medicine and Biology Society: 7541-7544

Kumaravelu K, Grill WM. 2024. Neural mechanisms of the temporal response of cortical neurons to intracortical microstimulation. Brain Stimulation 17: 365-381

Kumaravelu K, Sombeck J, Miller LE, Bensmaia SJ, Grill WM. 2022. Stoney vs. Histed: Quantifying the spatial effects of intracortical microstimulation. Brain Stimulation 15: 141-151

Lycke R, Kim R, Zolotavin P, Montes J, Sun Y, et al. 2023. Low-threshold, high-resolution, chronically stable intracortical microstimulation by ultraflexible electrodes. Cell Reports 42: 112554

Markram H, Muller E, Ramaswamy S, Reimann MW, Abdellah M, et al. 2015. Reconstruction and simulation of neocortical microcircuitry. Cell 163: 456-492

McIntyre CC, Grill WM. 2001. Finite element analysis of the current-density and electric field generated by metal microelectrodes. Annals of Biomedical Engineering 29: 227-235

Merrill DR, Bikson M, Jefferys JGR. 2005. Electrical stimulation of excitable tissue: design of efficacious and safe protocols. Journal of Neuroscience Methods 141: 171-198

Newman J. 1966. Resistance for flow of current to a disk. Journal of the Electrochemical Society 113: 501-502

O'Doherty JE, Lebedev MA, Ifft PJ, Zhuang KZ, Shokur S, et al. 2011. Active tactile exploration using a brain-machine-brain interface. Nature 479: 228-231

Raspopovic S, Capogrosso M, Petrini FM, Bonizzato M, Rigosa J, et al. 2014. Restoring natural sensory feedback in real-time bidirectional hand prostheses. Science Translational Medicine 6: 222ra19

Romo R, Hernández A, Zainos A, Brody CD, Lemus L. 2000. Sensing without touching: psychophysical performance based on cortical microstimulation. Neuron 26: 273-278

Romo R, Hernández A, Zainos A, Salinas E. 1998. Somatosensory discrimination based on cortical microstimulation. Nature 392: 387-390

Shadlen MN, Newsome WT. 1998. The variable discharge of cortical neurons: implications for connectivity, computation, and information coding. Journal of Neuroscience 18: 3870-3896

Sombeck JT, Heye J, Kumaravelu K, Goetz SM, Peterchev AV, et al. 2022. Characterizing the short-latency evoked response to intracortical microstimulation across a multi-electrode array. Journal of Neural Engineering 19: 026044

Tabot GA, Dammann JF, Berg JA, Tenore FV, Boback JL, et al. 2013. Restoring the sense of touch with a prosthetic hand through a brain interface. Proceedings of the National Academy of Sciences 110: 18279-18284

Urdaneta ME, Kunigk NG, Delgado F, Fried SI, Otto KJ. 2021. Layer-specific parameters of intracortical microstimulation of the somatosensory cortex. Journal of Neural Engineering 18: 055007

Wang B, Peterchev AV, Gaugain G, Ilmoniemi RJ, Grill WM, et al. 2024. Quasistatic approximation in neuromodulation. Journal of Neural Engineering 21: 041002

Wei XF, Grill WM. 2009. Analysis of high-perimeter planar electrodes for efficient neural stimulation. Frontiers in Neuroengineering 2: 15

Wiley, J.D. and Webster, J.G., 1982. Analysis and control of the current distribution under circular dispersive electrodes. *IEEE Transactions on Biomedical Engineering*, (5), pp.381-385.

Wu GK, Ardeshirpour Y, Mastracchio C, Kent J, Caiola M, Ye M. 2023. Amplitude- and frequency-dependent activation of layer II/III neurons by intracortical microstimulation. iScience 26: 108140